Nano Research

Open Access

Research Article

Innate and adaptive immune tolerance-inducing effects of extracellular vesicles derived from macrophages trained with low-dose LPS and self-antigen in spinal cord injury therapy

Tao Jia[1,2,§], Kunrong Xie[1,2,§], Jianing Zu[1], Jiawei Shen[1,2], Jiawen Niu[1,2], Xuefeng Li[1,2], Fawang Zhang[1,2], Hailong Zheng[3], Jinglong Yan[1] ✉, and Yufu Wang[1] ✉

[1] *Department of Orthopedic Surgery, Second Affiliated Hospital of Harbin Medical University, Harbin 150086, China*
[2] *Heilongjiang Provincial Key Laboratory of Hard Tissue Development and Regeneration, Harbin 150086, China*
[3] *Department of Orthopedic Surgery, The First People's Hospital of Yibin, Yibin 644000, China*
[§] *Tao Jia and Kunrong Xie contributed equally to this work.*

Cite this article: *Nano Research*, **2026**, *19*, 94908418. https://doi.org/10.26599/NR.2026.94908418

ABSTRACT: An imbalance between the innate and adaptive immunity after traumatic spinal cord injury (SCI) triggers excessive inflammatory activation, which ultimately leads to secondary neuronal damage and functional impairment. Importantly, inducing tolerance in both the innate and adaptive immunity helps suppress neuroinflammation and promotes neuroprotection. Innate immune tolerance triggered by lipopolysaccharides (LPS) is rapid, specific, and long-lasting; however, direct administration may cause significant side effects. Similarly, administering self-antigens after SCI can foster adaptive immune tolerance but may worsen tissue damage. Extracellular vesicles (EVs), as highly biocompatible natural carriers, address these challenges and deliver immunoregulatory signals to establish immune-tolerant microenvironments. Therefore, we preconditioned macrophages with a combination of low-dose LPS and self-antigens (myelin debris) to induce an immune-tolerant phenotype and isolated the resulting EVs trained with low-dose LPS and self-antigens (Trained-EVs). Our results demonstrate that Trained-EVs can effectively enhance innate immune tolerance and modulate adaptive immunity, thereby establishing a tolerogenic immune microenvironment. This dual strategy for inducing tolerance is a promising immunotherapeutic option for autoimmune and inflammatory diseases.

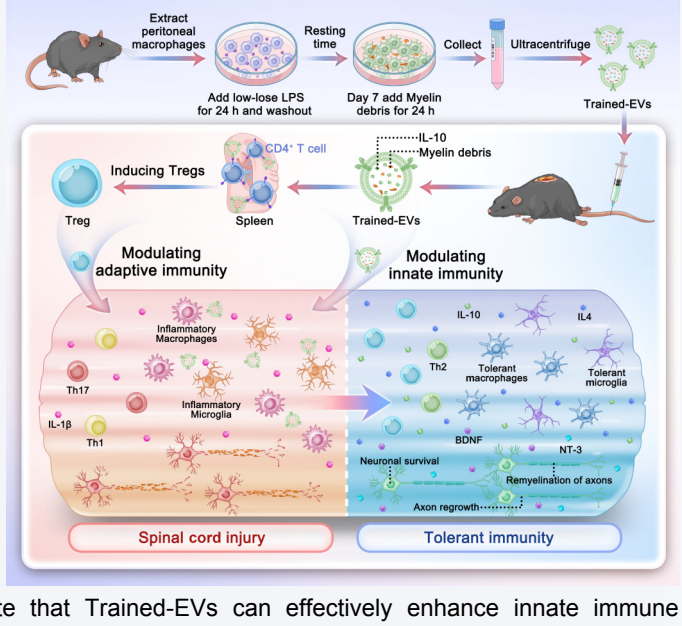

KEYWORDS: spinal cord injury, immune tolerance, extracellular vesicles, innate immunity, adaptive immunity

1 Introduction

Traumatic spinal cord injury (SCI) affects millions of people worldwide and often leads to irreversible disability and paralysis [1]. The evidence increasingly suggests that neuroinflammation after SCI is a key factor in secondary injury and significantly influences disease progression [2]. The inflammatory response following SCI is highly complex, and involves coordinated interactions between various immune cell types [3, 4]. Overactivation of innate immune cells, such as microglia and macrophages, contributes to neuronal loss and axon degeneration [5, 6], increasing the risk of neurological decline. Additionally, activation of adaptive immune cells, including T helper 1 (Th1)-type $CD4^+$ and $CD8^+$ T lymphocytes, further exacerbates demyelination and harms neurons and glia [7, 8].

Notably, both innate and adaptive immune cells contribute to protection by promoting immune tolerance [9]. In microglia,

Received: October 31, 2025; **Revised:** January 7, 2026
Accepted: January 8, 2026

✉Address correspondence to Jinglong Yan, yanjinglong2020@126.com; Yufu Wang, wangyufu@hrbmu.edu.cn

lipopolysaccharide (LPS)-induced tolerance reduces pro-inflammatory cytokine production and provides neuroprotection [10], a phenomenon observed in animal studies related to ischemic injury, Parkinson's disease, traumatic brain injury, spinal cord injury, and neuropsychiatric disorders [11–13]. Similarly, macrophage tolerance—induced by stimuli such as LPS or tumor necrosis factor (TNF)—is characterized by decreased secretion of pro-inflammatory mediators and increased expression of anti-inflammatory genes [14], reflecting an M2-like phenotype. Regulatory T cells (Tregs) are essential for maintaining the immune balance and preventing self-reactivity, and their dysfunction is linked to various immune-mediated and central nervous system disorders [15]. Therefore, inducing immune tolerance in these cells may help regulate the local immune environment and improve functional outcomes after SCI.

Although immune tolerance induction strategies for central nervous system (CNS) diseases have shown promise, their clinical application is limited by challenges such as complex induction protocols, excessive immunosuppression, and short-lived effects [16]. LPS-induced tolerance offers several benefits, including rapid onset, precise targeting, easy induction, and sustained efficacy, and has been studied in microglia using multiple animal models [17]. However, systemic LPS administration causes widespread distribution and may lead to adverse effects such as atherosclerosis, insulin resistance, and chronic obstructive pulmonary disease (COPD) [18, 19].

Tregs are essential for immune tolerance [20]. While adoptive Treg transfer can aid neurological recovery after SCI, excessive immunosuppression may paradoxically impair neuronal survival [21, 22]. Active immunization with self-antigens can promote Treg expansion and offer neuroprotection in some CNS diseases [23]; however, the results vary, with some studies demonstrating that the administration of myelin basic protein (MBP) after SCI can worsen tissue damage [24]. Therefore, the safe and effective induction of both innate and adaptive immune tolerance is crucial for the development of protective immunotherapies against SCI. As natural nanoscale vesicles, extracellular vesicles (EVs) are promising candidates for immune modulation [25]. By inheriting the membrane components from their parent cells, EVs exhibit excellent biocompatibility and low immunogenicity, allowing them to evade immune clearance and remain functionally active for long periods [26]. Macrophage-derived EVs can specifically target inflamed tissues, and their anti-inflammatory properties and ability to cross the blood–brain barrier (BBB) are well recognized [27]. In this study, EVs were isolated from macrophages preconditioned with low-dose LPS and exposed to self-antigens. This process mimics and enhances dynamic exposure to phagocytic antigens and inflammatory stimuli typical of the SCI microenvironment, thereby promoting immune tolerance in immune cells.

We demonstrated that EVs from trained macrophages promoted a tolerant phenotype in the innate immune system (macrophages and microglia) and enhanced the tolerogenic capacity of Tregs in the adaptive immune system. This approach avoids the risks associated with LPS or myelin debris (MD) by combining their advantages to create dual immunomodulatory effects. Our "preconditioning-regulation" dual tolerance induction strategy establishes a robust protective immune microenvironment that greatly supports neurological recovery and tissue repair in a mouse SCI model. These findings indicate that EV-based immunotherapy with multiple-target regulatory properties may be effective for SCI treatment.

2 Experimental

2.1 Reagents

Chemicals and kits included: LPS (L6143; Sigma-Aldrich, USA), Starch Broth (N8300; Solarbio, China), Pierce Chromogenic Endotoxin Quantitation Kit (A39552S; Thermo Fisher Scientific, USA), Nuclear Extract Kit (40010 & 40410; Active Motif, China), NF-κB p50 Transcription Factor Assay Kit (41096 & 41596; Active Motif, China), STAT3 Transcription Factor Assay Kit (45196 & 45696; Active Motif, China), IL-10 ELISA Kit (ML037873; Mlbio, China), IL-1β ELISA Kit (ML098416; Mlbio, China), IL-6 ELISA Kit (ML098430; Mlbio, China), TNF-α ELISA Kit (ML002095; Mlbio, China), NT-3 ELISA Kit (ML002111; Mlbio, China), BDNF ELISA Kit (ML002219; Mlbio, China), NGF ELISA Kit (ML002108; Mlbio, China), Estradiol ELISA Kit (PE223; Beyotime, China), Anti-mouse-CD86 PE (MA5-52362; Thermo Fisher Scientific, USA), Anti-mouse-CD206 FITC (MA5-16870; Thermo Fisher Scientific, USA), Anti-CD63 (Ab217345; Abcam, UK), Anti-Alix (Ab275377; Abcam, UK), Anti-TSG101 (Ab125011; Abcam, UK), Anti-Calnexin (Ab313243; Abcam, UK), Anti-IL-10 (12163S; Cell Signaling Technology, USA), Anti-IL-1β (12703S; Cell Signaling Technology, USA), Anti-IFN-γ (Ab280353; Abcam, UK), Anti-IL-4 (BS0581R; Bioss Antibodies, China), Anti-IL-17A (Ab302922; Abcam, UK), Anti-Foxp3 (12653S; Cell Signaling Technology, USA), Anti-CD4 (67786-1-Ig; Proteintech, China), Anti-iNOS (22226-1-AP; Proteintech, China), Anti-CD206 (24595S; Cell Signaling Technology, USA), Anti-F4/80 (71299S; Cell Signaling Technology, USA), Anti-neurofilament (NF) (2837S; Cell Signaling Technology, USA), Anti-GFAP (60190-1-Ig; Proteintech, China), Rabbit anti-NeuN (24307S; Cell Signaling Technology, USA), Goat anti-rat IgG (H+L) Alexa Fluor 647 (Ab150159; Abcam, UK), Goat anti-mouse IgG (H+L) Coralite 594 (SA00013-3; Proteintech, China), Goat anti-rabbit IgG (H+L) FITC (SA00003-2; Proteintech, China), Anti-rabbit IgG secondary antibody (ZF-0311; Zhongshan Jinqiao, China), 4',6-diamidino-2-phenylindole (DAPI) (C1006; Beyotime, China), Nissl Staining Kit (G1430; Solarbio, China), Intracellular Fixation & Permeabilization Buffer Set (Thermo Fisher Scientific, USA), Mouse Spleen Lymphocyte Isolation Kit (LTS1092PK; TBD, China), Lactate dehydrogenase (LDH) Assay Kit (WLA072a; Wanleibio, China), Alanine aminotransferase (ALT) Assay Kit (WLA114, Wanleibio, China); RAW264.7 mouse mononuclear macrophage leukemia cells (CL-0190; ProCell, China), BV2 mouse microglial cells (CL-0493; ProCell, China), and PC12 poorly differentiated rat adrenal pheochromocytoma cells (CL-0480; ProCell).

2.2 Mice

Female C57BL/6J mice aged 6–8 weeks were obtained from the Animal Experimental Center at the Second Affiliated Hospital of Harbin Medical University, Harbin, China. Female mice were selected for the study because they tend to have fewer postoperative complications than male mice, and it is easier to manually express the bladder after paralysis. All experimental procedures were approved by the Ethics Committee of the Harbin Medical University. The mice were housed in a specific pathogen-free (SPF) environment at the animal facility of Harbin Medical University.

2.3 Preparation and fluorescent labeling of myelin debris

Myelin debris was extracted as previously described [28, 29]. Mice

were anesthetized with 1.25% 2,2,2-tribromoethanol, followed by perfusion of 20 mL of pre-chilled 1× phosphate-buffered saline (PBS) into the cardiac circulation. Brain and spinal cord tissues were harvested and homogenized in a solution of 0.32 M sucrose dissolved in sterile water. The homogenate was placed on top of a 0.85 M sucrose solution to collect the sucrose interface (crude myelin membrane). This was diluted with sterile water at 4 °C before being centrifuged at 75,000*g* for 30 min at the same temperature. To induce hypo-oosmotic shock, cold sterile water was added at a volume 20 times that of the myelin component and the mixture was incubated on ice for 30 min. After resuspension, the sample was centrifuged again at 75,000*g* for 30 min and resuspended in a 0.32 M sucrose solution before a second layering onto a 0.85 M sucrose solution. A further centrifugation step at 75,000× *g* and 4 °C for 30 min was performed to concentrate the sample, after which the bottom membrane was diluted with cold sterile water. The sample was further concentrated by centrifugation at 75,000*g* at 4 °C, allowing for collection, lyophilization, and weighing of the 0.32/0.85 M sucrose interface membrane. Endotoxin levels were measured using a Pierce Chromogenic Endotoxin Quantitation Kit to ensure that they remained below 0.03 EU/mL. For cell culture, a concentration of 1.0 mg/mL of myelin debris was used. To label the debris with fluorescence, myelin was treated with the nontoxic dye carboxyfluorescein succinimidyl ester (CFSE). This dye passively diffuses into myelin and covalently bonds with the available amines. For labeling, 1 mg of myelin debris was combined with 50 μM CFSE and incubated at 37 °C for 15 min. The debris was centrifuged and washed with 100 mM glycine in PBS at 14,000 rpm for 15 min. This washing was repeated twice under the same conditions, after which the debris was collected and resuspended in PBS to a final volume of 100 μL for future experiments.

2.4 Cell culture and training protocols

Sterile starch broth was injected intraperitoneally into healthy mice. After 48 h, the mice were euthanized by cervical dislocation and immersed in 75% ethanol, and a midline abdominal incision was made to expose the peritoneal cavity under sterile conditions. A total of five milliliters of precooled sterile 1× PBS was gradually introduced into the peritoneal cavity, followed by gentle abdominal massage for 1 min to facilitate peritoneal lavage fluid recovery, which was collected using a sterile pipette. The samples were centrifuged at 850 rpm for 5 min, and the supernatant was discarded. The resulting pellet was resuspended in Dulbecco's modified eagle medium (DMEM) supplemented with 10% fetal bovine serum (FBS), plated onto 10-cm culture dishes, and incubated for 2 h. Non-adherent cells were removed, and the primary macrophages were divided into three groups: a control group (no stimulation), a low-dose LPS group (1 ng/mL), and a high-dose LPS group (1 μg/mL). After a 24-h culture, the LPS-containing medium was replaced with PBS and the cells were washed three times. The medium was refreshed every two days. On day 7, myelin debris (1 mg/mL) was added to each group and the cells were incubated for another 24 h. Finally, the cells and supernatants were collected for further analysis. All experiments were performed under sterile conditions and each experiment was conducted in triplicate.

2.5 Isolation of extracellular vesicles

The EV isolation method is based on a previously described procedure [30]. First, the culture supernatants were subjected to sequential centrifugation at 300*g* for 10 min, then at 2000*g* for 20 min, and 10,000*g* for 30 min to remove cellular debris. The resulting supernatant was filtered through a 0.22-μm filter and then ultracentrifuged at 110,000*g* for 70 min (Himac CP100NX; Hitachi, Japan) to pellet the EVs. The supernatant was removed, and the pellet was resuspended in PBS. This suspension was ultracentrifuged again at 110,000*g* for 70 min to obtain purified EVs. The purified EVs were then resuspended in PBS, divided into aliquots, and stored at −80 °C until needed.

2.6 Characterization of extracellular vesicles

An EV suspension of 10 μL was diluted in 1 mL of PBS, thoroughly mixed, and then analyzed using a nanoparticle tracking analysis (NTA) system (Particle Metrix GmbH, Germany). Each sample was analyzed in triplicate. Using ZetaView software (v8.04.02), particle concentration, size distribution, and average diameter were determined, with results reported as mean ± standard deviation (SD). For transmission electron microscopy (TEM), 10 μL of the EV suspension was applied to a carbon-coated copper grid and incubated at room temperature for 5 min. Excess liquid was removed with a filter paper, followed by negative staining with 2% phosphotungstic acid (pH 7.0) for 2 min. After air-drying, the samples were examined by TEM (Hitachi, Japan). Random fields were imaged to assess the morphology and size of EVs.

For western blotting (WB) analysis, total protein from EVs was extracted and its concentration was measured using the bicinchoninic acid (BCA) assay. A total of 30 μg of protein was separated by 10% sodium dodecyl sulfate-polyacrylamide gel electrophoresis (SDS-PAGE) at 100 V for 90 min, then transferred to polyvinylidene fluoride (PVDF) membranes. Blocking was performed with 5% skim milk at room temperature for 1 h, followed by overnight incubation at 4 °C with primary antibodies (anti-CD63, anti-Alix, anti-TSG101, and anti-calnexin). After three washes with Tris-buffered saline with Tween 20 (TBST) (10 min each), the membranes were incubated with horseradish peroxidase-conjugated secondary antibodies for 1 h at room temperature. The signals were visualized using an electrochemiluminescence (ECL) substrate and imaged.

2.7 Analysis of vesicle proteins and microglia phenotype by western blotting

Total proteins from EVs and microglia were extracted, and subsequent steps were performed as described previously. Primary antibodies (anti-IL-10, anti-IL-1β, anti-CD86, and anti-CD206) were used for incubation, and membranes were developed with an ECL substrate kit before image acquisition.

2.8 Extraction of nuclear proteins and transcription factor activity assay

Nuclear proteins from macrophages, microglia, and spinal cord tissue were extracted using an active motif nuclear extraction kit. Protein concentrations were measured using the BCA assay, then aliquoted and stored at −80 °C. The activities of nuclear factor kappa-light-chain-enhancer of activated B cells (NF-κB) p50 and signal transducer and activator of transcription 3 (STAT3) were measured in 20 μg of nuclear protein from each group, using the relevant Active Motif Transcription Factor Assay Kits.

2.9 The enzyme-linked immunosorbent assay (ELISA)

Supernatants were collected from macrophages and microglia in all

groups and centrifuged at 12,000× *g* for 10 min to remove impurities. Peripheral blood was collected from the tail vein of the mice at different time points for serum separation. The levels of interleukin-1*β* (IL-1*β*), IL-10, IL-6, TNF-*α*, brain-derived neurotrophic factor (BDNF), neurotrophin-3 (NT-3), nerve growth factor (NGF) and 17-*β*-estradiol (E2) were measured using ELISA kits.

2.10 RNA isolation and reverse transcription quantitative polymerase chain reaction (RT-qPCR) analysis

Total RNA was extracted from each group using TRIzol reagent and analyzed by RT-qPCR. Quantitative PCR was performed using the Stratagene Mx3005p Real-Time PCR System (Agilent Technologies, USA). The primer sequences are listed in Table S1 in the Electronic Supplementary Material (ESM).

2.11 Library preparation and RNA sequencing analysis

Total RNA samples were sent to OE Biotech Co., Ltd. (Shanghai, China) for library construction and sequencing. Differential expression analysis was conducted using DESeq2, with significance thresholds set at $P < 0.05$ and fold change > 2 or < 0.5. Gene Ontology (GO) and Kyoto Encyclopedia of Genes and Genomes (KEGG) pathway enrichment analyses were performed on the identified differentially expressed genes (DEGs), and enrichment was evaluated using normalized enrichment score (NES) and false discovery rate (FDR) values.

2.12 Luminex multiplex cytokine assay

Total spinal cord samples collected at days 3 and 7 post-injury were sent to LabEx Biotech Co., Ltd. (Shanghai, China) for multiplex cytokine analysis using Luminex technology.

2.13 SCI model

The SCI model was implemented as previously described. Mice were randomly assigned to four groups: Trained-EVs, MD-EVs, EVs, and PBS. Anesthesia was administered via an intraperitoneal injection of 1.25% 2,2,2-tribromoethanol (Nanjing Aibei Biotechnology Co., Ltd.) at a dose of 0.01 mL per gram of body weight. Once the mouse lost consciousness, a midline incision was made under sterile conditions to expose and remove the lamina at the T10 level, thereby revealing the spinal cord. SCI was induced using a heavy object drop apparatus (RWD Life Science), which involved releasing a 5 g impact rod from a height of 5 cm to strike the exposed T10 spinal cord vertically. The muscle and skin were sutured in layers, and manual bladder expression was performed twice daily after surgery. Two hours after the SCI, mice received an intravenous injection of 100 μg of vesicles in 100 μL of PBS; the control group received the same volume of PBS.

2.14 *In vivo* tracking of vesicle distribution

EVs from each group were labeled with DiR fluorescent dye by incubating 100 μg of EVs in a 5 μM DiR solution for 30 min in the dark. Two hours after injury modeling, DiR-labeled EVs were injected intravenously through the tail vein. At 24 h post-injection, the fluorescence in various organs, including the liver, heart, spleen, lungs, kidneys, and spinal cord, was imaged using an *in vivo* imaging system.

2.15 Flow cytometry

BV2 and RAW264.7 cells from different treatment groups were collected and subjected to digestion with 0.25% trypsin, then resuspended in PBS to form a single-cell suspension at a concentration of 1×10^6 cells/mL. An aliquot of 100 μL from this suspension was incubated in the dark for 30 min with CD86-PE or CD206-FITC antibodies.

Mouse spleens were carefully harvested under aseptic conditions. According to the manufacturer's instructions, lymphocytes were isolated using a commercial kit designed for mouse splenic lymphocyte isolation. The cells were washed with PBS and resuspended at a density of 1×10^6 cells/mL. After fixation and permeabilization, the cells were labeled with flow cytometry antibodies, including anti-mouse CD3-FITC, CD3-PerCP-Cyanine5.5, CD4-PE, IFN-*γ*-FITC, IL-4-APC, IL-17A-PerCP-Cyanine5.5, CD25-APC, and FoxP3-PE, with staining conducted in the dark for 30 min. The samples were analyzed using a flow cytometer (A60-Universal; ApogeeFlow, England), and the resulting data were analyzed using FlowJo v10.8.1.

2.16 Fixation and sectioning of spinal cord tissue

Mice with SCI were anesthetized following established protocols and underwent transcardial perfusion with 4% paraformaldehyde followed by saline. After euthanasia, spinal cord tissues were collected for both frozen and paraffin-embedded sectioning. For frozen sections, a 10-mm segment of the spinal cord centered on the injury site was excised and fixed overnight in 4% paraformaldehyde. The next day, the tissue was dehydrated using a graded series of sucrose solutions (10%, 20%, and 30%) until fully submerged. After embedding in optical coherence tomography (OCT), the tissue was preserved at −80 °C, sliced into 5-μm cross-sections with a cryostat, mounted on poly-L-lysine-coated slides, and stored at −80 °C until needed. For paraffin sections, a 10-mm segment of the spinal cord centered on the injury site was isolated, fixed in 4% paraformaldehyde, and embedded in paraffin. Once embedded, the tissue was sectioned into 5-μm slices.

2.17 Immunofluorescence

PC12 cells were seeded in the lower chamber of a Transwell insert pre-coated with sterile coverslips and treated according to the specified experimental conditions. The cells were fixed at room temperature with 4% paraformaldehyde for 15 min and permeabilized with 0.1% Triton X-100 for 10 min. A working solution of Actin-Tracker Green-488 (diluted in PBS containing 3% BSA and 0.1% Triton X-100) was added and the cells were incubated at room temperature for 60 min. After staining with DAPI for 4 min, the coverslip was carefully removed, air-dried, and mounted onto a glass slide. PBS washes were performed in triplicate, each lasting 5 min.

Frozen sections were brought to room temperature and then fixed with 4% paraformaldehyde at 4 °C for 15 min. The sections were then permeabilized with 0.3% Triton X-100 for 10 min. After a 30-min blocking step at room temperature using 5% BSA, primary antibodies, including F4/80, Iba-1, iNOS, CD206, CD4, IFN-*γ*, IL-17A, IL-4, FoxP3, NF, and glial fibrillary acidic protein (GFAP), were applied and incubated overnight at 4 °C. After the PBS washes, the appropriate secondary antibodies were added and incubated in darkness at 37 °C for 1 h. The samples were then stained with DAPI for 5 min and mounted using an anti-fade reagent. Fluorescence images were captured using a confocal laser scanning microscope (LSM800; Zeiss, Germany) and quantitative data were collected from randomly selected microscopic fields across five samples.

2.18 Immunohistochemistry

Cross-sections of the spinal cord embedded in paraffin were deparaffinized, rehydrated, and incubated for 10 min at room temperature with 3% H_2O_2 to inhibit endogenous peroxidase activity. Antigen retrieval was performed by heating the sections in citrate buffer (pH 6.0) for 15 min. After cooling naturally, the sections were washed three times with PBS. Tissue sections were incubated for 30 min at room temperature with 5% BSA to block nonspecific binding sites, then incubated overnight at 4 °C with a rabbit anti-mouse NeuN antibody. Next, a goat anti-rabbit secondary antibody was applied and incubated at room temperature for 1 h. The 3,3'-Diaminobenzidine (DAB) chromogenic reaction was conducted for 5–10 min, after which hematoxylin counterstaining was performed for 30 s. The sections were differentiated using acid-alcohol, blued with ammonia water, dehydrated using graded ethanol solutions, cleared with xylene, and mounted in a neutral resin. From each mouse within the experimental groups, five sections were randomly chosen, and dendritic complexity, defined as the dendritic area of surviving neurons at the center of the SCI lesion, was evaluated.

2.19 Nissl staining

Cross-sections of the spinal cord in paraffin were processed using a Nissl staining kit following the manufacturer's protocol. The sections were deparaffinized and rehydrated before being incubated in a cresyl violet staining solution at 56 °C for 1 h in a controlled-temperature incubator. After rinsing with distilled water, the sections were differentiated in Nissl differentiation solution for 2 min, dehydrated with absolute ethanol, cleared with xylene, and mounted on slides with neutral resin. Five stained sections were randomly selected from each mouse in the experimental group, and the average number of neurons with intact Nissl bodies at the center of the SCI lesion was recorded.

2.20 TEM of spinal cord myelin

Spinal cords from dissected mice, each measuring 10 mm in length and located at the center of the injury epicenter, were preserved in a 2.5% glutaraldehyde solution at 4 °C for 24 h. This was followed by a 2-h immersion in 2% osmium tetroxide. The tissues underwent dehydration, standard embedding procedures, and were then sliced transversely into 5-μm sections. The sections were stained with 0.5% toluidine blue and analyzed using a transmission electron microscope (Hitachi, Japan).

2.21 Basso mouse scale (BMS)

The BMS was used to assess hind limb motor function in the SCI mice. The scores ranged from 0 (complete paralysis with no hind limb movement) to 9 (normal coordinated gait with proper paw placement). Assessments were conducted in a quiet environment by placing the mice on a smooth surface (40 cm × 60 cm) for continuous observation over 5 min. Two independent blinded observers scored left and right hind limb function separately. The final score for each hind limb was the average of the scores of the two observers, and the overall BMS score for each mouse was the average of the hind limb scores. Assessments were performed at 0, 1, 3, 7, 14, 21, 28, and 35 dpi with at least five mice per group.

2.22 Catwalk-assisted gait analysis

Gait function was quantitatively measured at 35 dpi using the CatWalk XT system (Noldus Information Technology, Netherlands). Mice completed three days of acclimation training before testing to ensure voluntary crossing of the walkway. During testing, the mice were placed at the start of the CatWalk runway and their gait videos were recorded as they voluntarily moved across the transparent walkway. Three valid trials were performed for each mouse.

2.23 Drug toxicity assays

Twenty-four hours post-injection of EVs via the tail vein, tissues from the heart, liver, spleen, lungs, and kidneys were collected, fixed in 4% paraformaldehyde, and embedded in paraffin. Sections of 4-μm thickness were prepared by dewaxing with xylene, followed by rehydration through graded ethanol washes and rinsing with distilled water. The sections were stained with hematoxylin for 2 min and then rinsed with running water for 5 min to produce blue nuclei. Next, differentiation was performed in 1% hydrochloric acid-ethanol for 30 s, followed by counterstaining with eosin for 1 min. After dehydration using graded ethanol solutions and clearing with xylene, the slides were covered with coverslips. Images were captured by randomly selecting five fields per group using an electron microscope. Lactate dehydrogenase (LDH) and alanine aminotransferase (ALT) activities were measured using commercial assay kits. Absorbance values (optical density (OD)) were recorded with a microplate reader and analyzed statistically.

2.24 Statistics analysis

Statistical analyses and graph creation were performed using SPSS and GraphPad Prism software. Data are presented as the mean ± SD. Unpaired two-tailed t-tests were used to compare two groups. For comparisons involving more than two groups, one-way analysis of variance (ANOVA) was performed. For data with repeated measures across multiple groups, a two-way repeated-measures (RM) ANOVA was applied. $P < 0.05$ was considered statistically significant ($^*P < 0.05$, $^{**}P < 0.01$, $^{***}P < 0.001$, $^{****}P < 0.0001$).

3 Results

3.1 Preparation and characterization of Trained-EVs

Myelin debris, acting as an autoantigen, induces Treg generation and provides neuroprotection in some CNS diseases but may worsen tissue damage after SCI. Macrophages pretreated with low-dose LPS show significantly reduced inflammatory responses and develop immune tolerance upon re-stimulation, whereas LPS alone carries potential biotoxicity risks [31]. To address these limitations, we devised a "preconditioning-regulation" strategy and examined the effects of sequentially administering different doses of LPS followed by myelin debris on macrophages. Macrophages were initially treated with either high-dose LPS (1 μg/mL) or low-dose LPS (1 ng/mL) for 24 h, then washed and medium replaced every two days. On day 7, myelin debris (1 mg/mL) was added to all groups for another 24 h incubation (Fig. 1(a)). The experimental groups are shown in Fig. 1(b). Cells and supernatants were collected for analysis of IL-10 and IL-1β mRNA and protein expression using RT-qPCR and ELISA, respectively. Data analysis revealed that the group treated with low-dose LPS followed by MD had significantly higher levels of IL-10 mRNA and protein than both the MD-only group and high-dose LPS + MD denticulata groups. Meanwhile, IL-1β mRNA and protein expression are notably decreased in this group (Figs. 1(c) and 1(d)), indicating that sequential

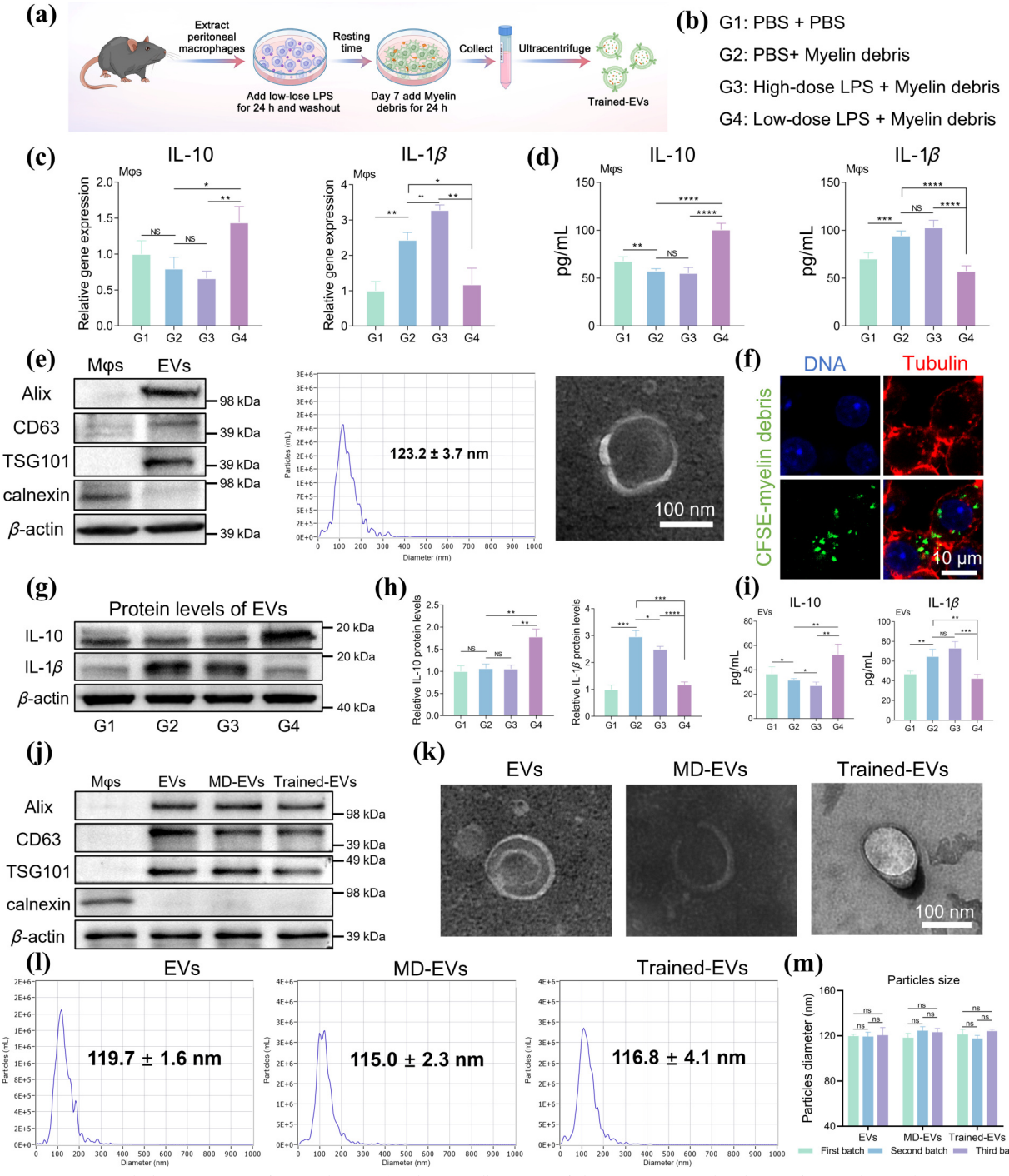

Figure 1 Preparation and characterization of Trained-EVs. (a) Schematic illustration of the preparation and isolation of Trained-EVs. (b) Diagram shows the experimental grouping. (c) RT-qPCR analysis indicating the gene expression levels of IL-10 and IL-1β in the different groups (n = 3, mean ± SD). (d) ELISA was used to measure the protein levels of IL-10 and IL-1β in each group (n = 4, mean ± SD). (e) Western blotting, NTA, and TEM characterizing the successful isolation of extracellular vesicles (scale bar = 100 nm). (f) Macrophages effectively uptake CFSE-labeled myelin debris (scale bar = 10 μm). (g, h) Western blot assessment and quantitative analysis of IL-10 and IL-1β levels in extracted vesicles (n = 3, mean ± SD). (i) ELISA quantifies IL-10 and IL-1β in isolated EVs (n = 4, mean ± SD). (j) Western blot confirming the presence of positive markers Alix, TSG101, and CD63, along with the absence of the negative marker Calnexin. (k) The ultrastructure of EVs is shown in TEM images (scale bar = 100 nm). (l) NTA analysis displaying EV size distribution (n = 3). (m) The bar chart shows that there is no significant difference in particle size of EVs among different batches in each group (n = 3, mean ± SD). One-way ANOVA with Tukey's post hoc test assessed statistical significance. ns indicates not significant. $^{*}P < 0.05$, $^{**}P < 0.01$, $^{***}P < 0.001$, $^{****}P < 0.0001$.

administration of low-dose LPS and MD effectively reprograms macrophage immune responses. EVs were isolated from the supernatants of treated macrophages and characterized using a series of assays, confirming successful extraction (Fig. 1(e)).

Furthermore, phagocytosis assays showed that CFSE-labeled myelin debris were effectively engulfed by macrophages (Fig. 1(f)). Although variations in the immune responses of macrophages under different treatments are well-known, functional changes in

EVs, which serve as key mediators of intercellular communication, remain unclear under various conditions. To explore this, we isolated EVs from the supernatants of cells treated under four different conditions: PBS, MD, high-dose LPS + MD, and low-dose LPS + MD. These EVs were then analyzed for IL-10 and IL-1β protein levels using WB and ELISA. The results showed significant differences between the two groups. Trained-EVs from the low-dose LPS + MD group exhibit notably higher IL-10 protein levels and significantly lower IL-1β protein levels compared to the other groups (Figs. 1(g)–1(i)).

To further investigate the structural and functional differences in EVs under various treatments, we isolated EVs the PBS, MD, and low-dose LPS combined with MD (Trained) groups and examined the expression of Alix, CD63, TSG101, and calnexin using WB, complemented by TEM and NTA for comprehensive characterization (Figs. 1(j)–1(l)). Figure S17 in the ESM (TEM) shows multiple EVs with uniform spherical morphology. Notably, NTA confirmed a consistent size distribution for EVs in each group across three independent batches, with an average diameter of ~ 120 nm and no significant inter-batch differences, demonstrating high reproducibility of the EV preparation (Fig. 1(m), and Fig. S18(b) in the ESM).

3.2 Transcriptomic changes in microglia induced by Trained-EVs and the mechanisms of immune tolerance

Previous studies have confirmed that macrophages and microglia exhibit strong pro-inflammatory phenotypes after SCI, which worsen neurological dysfunction [32]. As immune cells reside in the spinal cord, microglia play a crucial role in controlling the initial inflammatory response following SCI [33].

To determine whether Trained-EVs induce immune tolerance in pro-inflammatory microglia, BV2 cells were treated with a high concentration of LPS (1 μg/mL) for 24 h to simulate the inflammatory environment [34, 35]. The cells were then divided into PBS control and Trained-EVs groups, and gene expression differences were analyzed via RNA-seq. Compared to PBS, Trained-EVs-treated BV2 cells show significant transcriptional changes, with 144 genes upregulated and 139 downregulated (Fig. 2(a)). GO enrichment analysis of the top 20 downregulated genes revealed significant enrichment in the immune response, inflammatory response, cytokine activity, and interleukin-1 receptor binding pathways (Fig. 2(b)). Specifically, inflammatory response (GO:0006954, NES = −1.95, FDR = 0.031) and immune response (GO:0006955, NES = −2.2, FDR = 0.002) genes were notably downregulated in the Trained-EVs group (Fig. 2(d)), indicating effective suppression of inflammation and immune activation in BV2 cells. Meanwhile, KEGG analysis of the top 20 downregulated pathways highlights significant enrichment of classical inflammatory signaling pathways, including NF-κB, JAK-STAT, TNF, and IL-17 (Fig. 2(c)). Complementary GSEA further confirmed the widespread downregulation of key pathways, including NF-κB (mmu04064, NES = −2.05, FDR = 0.001) and JAK-STAT (mmu04630, NES = −1.55, FDR = 0.083), in the Trained-EVs group (Fig. 2(e)).

To validate the changes in signaling activity, we examined the transcriptional activities of NF-κB p50 and STAT3. Both were significantly reduced in Trained-EVs compared to those in PBS and controls (Fig. 2(f)), which aligns with the pathway enrichment analysis. These findings indicate that Trained-EVs inhibit BV2 cell inflammatory responses by targeting key transcription factors, thereby blocking upstream pro-inflammatory signaling pathways such as NF-κB and JAK-STAT. Consistent with GSEA and KEGG pathway analyses, Trained-EVs significantly reduced the transcriptional activities of NF-κB p50 and STAT3 in LPS-activated microglia, directly demonstrating suppression of these key inflammatory signaling pathways (Figs. S7 and S8 in the ESM). Moreover, western blotting and ELISA results (Figs. 1(g)–1(i)) revealed that Trained-EVs are enriched in IL-10, a cytokine known to inhibit NF-κB and JAK-STAT signaling and promote immune tolerance [36, 37]. These findings are consistent with previous reports that modulation of NF-κB and STAT3 signaling underlies endotoxin tolerance in macrophages [14, 35]. A heatmap of inflammation-related DEGs shows that Trained-EVs significantly upregulate anti-inflammatory and immune tolerance genes like Arg-1 and CD206, while pro-inflammatory genes like IL-1α, IL-1β, and IL-6 are notably downregulated (Fig. 2(g)). These results highlight the bidirectional regulatory effects of Trained-EVs on BV2 cell gene expression, supporting the earlier pathway enrichment findings. They further confirmed that Trained-EVs reprogrammed BV2 cell transcriptomic profiles, shifting cells from a pro-inflammatory phenotype toward immune tolerance.

To validate the regulatory effects at the protein and phenotypic levels, flow cytometry, WB, and ELISA were performed on BV2 cells. Flow cytometry showed that CD86 expression significantly decreased, whereas CD206 expression markedly increased in Trained-EVs compared to PBS (Figs. 2(h) and 2(i)). These results indicated that Trained-EVs modulated BV2 cell phenotypes, promoting a shift toward an anti-inflammatory state. Densitometric WB analysis confirmed this trend, showing decreased CD86 and increased CD206 expression in Trained-EVs compared to PBS (Fig. 2(j)). ELISA indicated that pro-inflammatory cytokines TNF-α, IL-1β, and IL-6 are reduced, while anti-inflammatory IL-10 was elevated after trained-EV treatment compared to PBS (Fig. 2(k)). These results aligned with the RNA-seq data, confirming at the cytokine secretion level that Trained-EVs suppress inflammation and promote immune tolerance. TEM revealed that BV2 cells treated with Trained-EVs exhibited a typical M2-like tolerant morphology, characterized by increased and elongated filopodia (Fig. S1 in the ESM).

Taken together, these findings show that Trained-EVs effectively cause proinflammatory BV2 cells to shift toward immune tolerance. This change was validated by evidence at the gene transcription, signaling, protein expression, and cellular morphology levels, highlighting the important role of Trained-EVs in regulating immune responses in inflammatory microenvironments.

3.3 Trained-EVs induce neurorestorative and regenerative effects in microglia *in vitro*

RNA-seq analysis further demonstrated that the Trained-EVs induced neurorestorative and regenerative effects in BV2 cells. Heatmap analysis of the RNA-seq data showed that, compared to PBS, Trained-EVs significantly upregulated neuroregeneration-related genes, including *Arg-1* and *Igf1* (Fig. 3(a)). KEGG pathway analysis of the upregulated genes revealed significant enrichment of the axon guidance pathway among the top 10 enriched pathways (Fig. 3(b)). GSEA confirmed an overall upward trend in the axon guidance pathway (mmu04360, NES = 0.85, FDR = 1.0) in the trained-EV group, along with significant enrichment and upregulation of the neurotrophin signaling pathway (mmu04722, NES = 1.38, FDR = 0.692) (Figs. 3(c) and 3(d)). The axon guidance

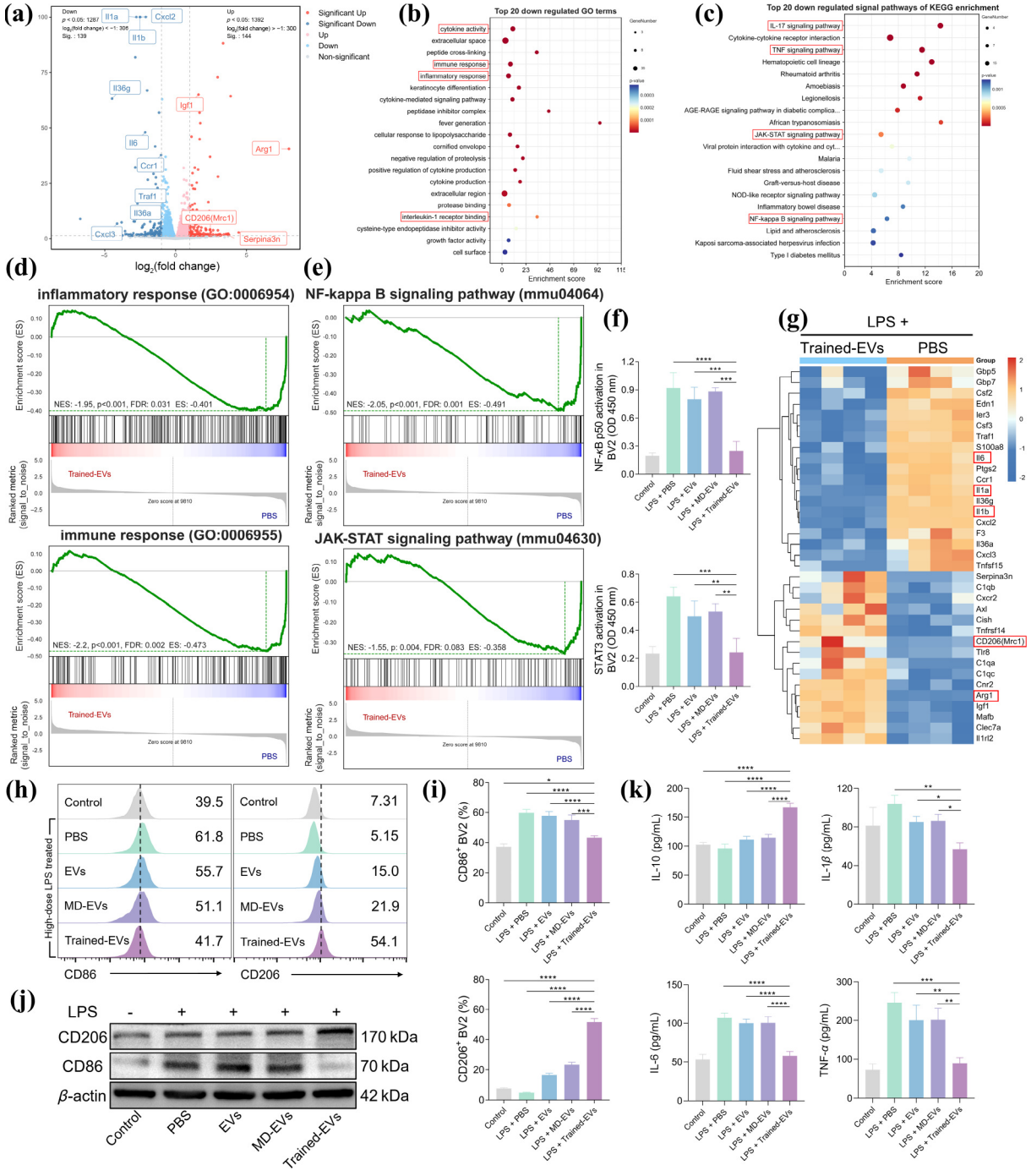

Figure 2 Transcriptomic changes in microglia induced by Trained-EVs and mechanisms of immune tolerance. (a) The volcano plot shows genes that are differentially expressed when comparing the Trained-EVs and PBS groups in an inflammatory context. (b) GO enrichment analysis indicates that downregulated DEGs are significantly enriched in pathways related to immune response and inflammation, as shown by the top 20 terms. (c) KEGG pathway enrichment analysis identifies significantly downregulated inflammatory signaling pathways (top 20 pathways). (d) and (e) GSEA reveals significant suppression of inflammatory response, immune response, NF-κB, and JAK-STAT signaling pathways. (f) NF-κB p50 and STAT3 transcriptional activities are quantified in BV2 cells under inflammatory conditions (n = 3, mean ± SD). (g) Heatmap shows expression profiles of inflammation-associated DEGs between Trained-EVs and PBS groups (n = 4). (h) and (i) Flow cytometry and quantitative analysis demonstrate immunophenotypic shifts in BV2 cells toward an anti-inflammatory profile (n = 3, mean ± SD). (j) Western blotting was performed on BV2 cells stimulated with high-dose LPS. (k) ELISA quantifies TNF-α, IL-1β, IL-6, and IL-10 protein concentrations in culture supernatants across groups (n = 3, mean ± SD). $^{*}P < 0.05$, $^{**}P < 0.01$, $^{***}P < 0.001$, $^{****}P < 0.0001$.

pathway is essential for directing neuronal axonal growth. Trained-EVs promote neurorestoration and regeneration at the transcriptional level through activation of this pathway. RT-qPCR showed that compared to PBS, Trained-EVs significantly increased the mRNA levels of BDNF and NT-3 in BV2 cells (Fig. 3(e)). ELISA further confirmed significantly higher secretion of BDNF and NT-3 by BV2 cells in the Trained-EVs group than in the PBS group (Fig. 3(f)).

Rat pheochromocytoma cells (PC12), which express high levels of NGF receptors, are commonly used for axonal growth assays.

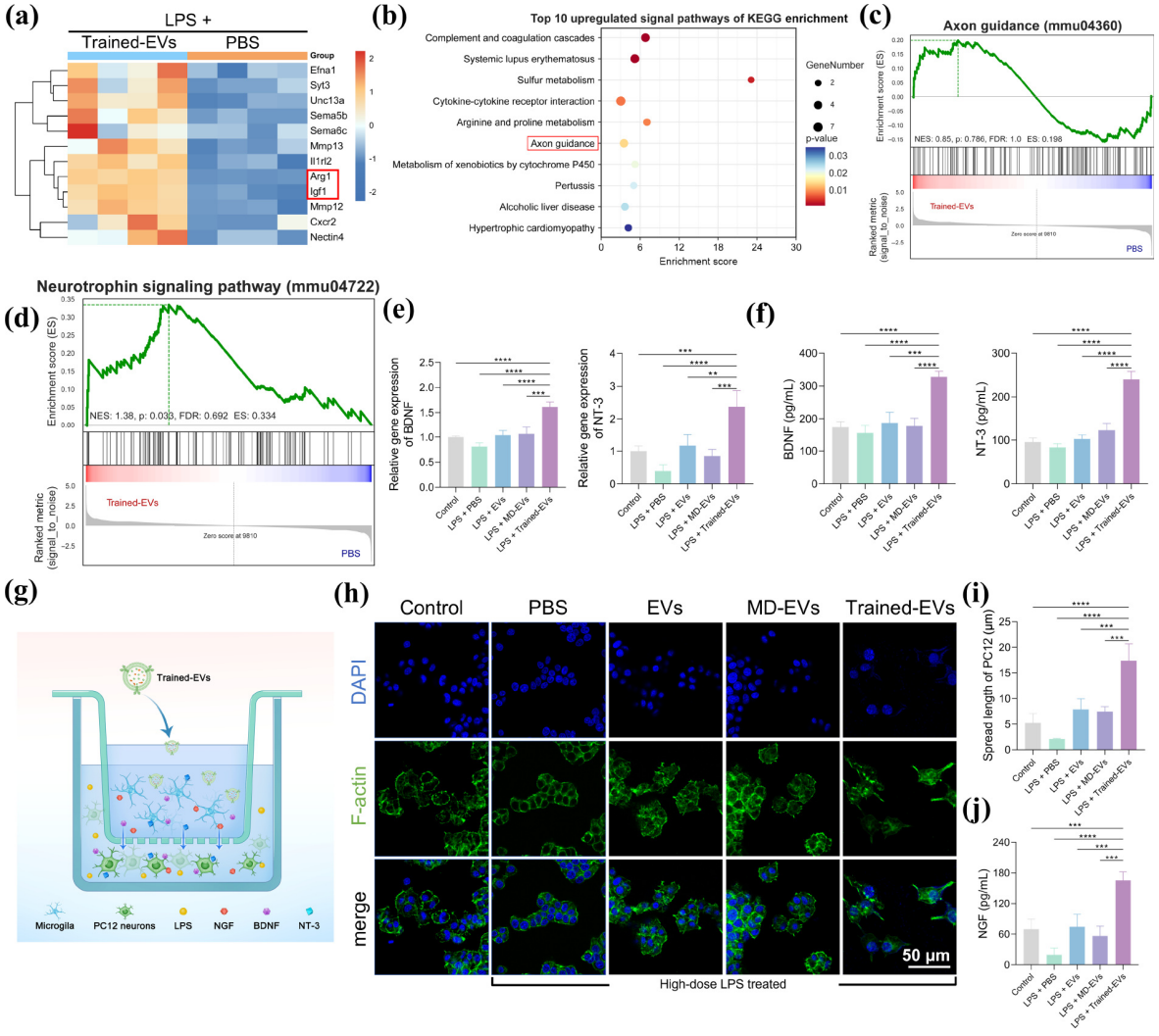

Figure 3 Trained-EVs promote neurorestorative and regenerative effects in microglia *in vitro*. (a) Heatmap of DEGs related to neurorestoration and regeneration between Trained-EVs and PBS groups under inflammatory conditions ($n = 4$). (b) GO enrichment analysis showing upregulated DEGs (top 10 terms). (c) and (d) GSEA indicates enrichment in axon guidance and neurotrophin signaling pathways. (e) RT-qPCR displays the expression levels of BDNF and NT-3 genes in BV2 cells subjected to different treatment groups ($n = 3$, mean ± SD). (f) ELISA measures BDNF and NT-3 protein levels across different groups under inflammatory conditions ($n = 3$, mean ± SD). (g) Schematic illustration of the Transwell co-culture system of BV2 and PC12 cells. (h) Measurement and (i) statistical analysis show neurite length in PC12 cells cultured under pathological conditions with various BV2 cell treatments ($n = 3$, mean ± SD, scale bar = 50 μm). (j) ELISA quantifies NGF secretion levels in the supernatant from the upper Transwell chamber containing BV2 cells ($n = 3$, mean ± SD). $^{*}P < 0.05$, $^{**}P < 0.01$, $^{***}P < 0.001$, $^{****}P < 0.0001$.

Inflammatory conditions inhibit under inflammatory conditions [38]. To examine the effect of Trained-EVs on axonal growth during inflammation, a Transwell co-culture system was established. Low-differentiated PC12 cells were seeded in the lower chamber with high-dose LPS (1 μg/mL) to mimic inflammation. The BV2 cells were seeded in the upper chamber and treated with EVs or PBS (Fig. 3(g)). After 24 h of co-culture, the average neurite length of PC12 cells in the Trained-EVs group reached 15 μm (Figs. 3(h) and 3(i)), greatly surpassing other groups. Additionally, ELISA of the BV2 cell supernatant showed that Trained-EVs increased NGF secretion (Fig. 3(j)), which supports axonal growth. This finding is consistent with previous sequencing and immunofluorescence data.

These findings suggest that Trained-EVs play a key role in neurorestoration and regeneration, promoting axonal growth in PC12 cells under inflammatory conditions by regulating BV2 cell function.

3.4 Trained-EVs induce transcriptional changes and immune tolerance mechanisms in macrophages *in vitro*

During the pathological process of SCI, microglia and blood-derived macrophages share roles in regulating inflammation. However, macrophages contribute more to injury clearance because of their stronger phagocytic ability. Nevertheless, excessive macrophage activation can trigger pro-inflammatory responses that worsen neurological dysfunction [29, 39]. To create an inflammatory model and evaluate the immunoregulatory effects of Trained-EVs on inflammatory macrophages, the RAW264.7 mouse macrophage cell line was exposed to a high dose of LPS (1 μg/mL) for 24 h [40].

Electron microscopy (EM) showed that cells in the PBS group had irregular amoeboid shapes with short, thick pseudopodia, typical of a pro-inflammatory phenotype. In contrast, the cells in the Trained-EV group showed significantly more and longer filopodia (Fig. S2 in the ESM). RNA-seq was used to compare the

gene expression profiles between the PBS- and Trained-EV groups. The results revealed notable gene expression changes with 224 upregulated genes and 374 downregulated genes in the trained-EV group compared to the PBS group (Fig. S3 in the ESM). GO pathway analysis of the top 20 downregulated genes revealed significant enrichment in the immune response, inflammatory response, and cytokine activity pathways (Fig. S4 in the ESM). GSEA confirmed the significant downregulation of gene sets related to the inflammatory response (GO:0006954, NES = −2.58, FDR < 0.001) and immune response (GO:0006955, NES = −2.48, FDR < 0.001) (Fig. S5 in the ESM). Additionally, KEGG pathway analysis of the top 20 downregulated pathways showed clear suppression of key inflammatory signaling pathways, including NF-κB, JAK-STAT, TNF, and IL-17 (Fig. S6 in the ESM). Complementary GSEA further validated the widespread downregulation of key signaling pathways, such as NF-κB (mmu04064, NES = −2.27, FDR < 0.001) and JAK-STAT (mmu04630, NES = −2.42, FDR < 0.001), in the Trained-EVs group (Fig. S7 in the ESM). Transcription factor activity assays indicated significant reductions in NF-κB p50 and STAT3 activities in the Trained-EVs group (Fig. S8 in the ESM). A heatmap of differentially expressed inflammatory genes showed marked downregulation of pro-inflammatory genes, including IL-1α, IL-1β, and IL-6, in the Trained-EVs group (Fig. S9 in the ESM).

Flow cytometry and ELISA analyses demonstrated that the Trained-EVs decreased the pro-inflammatory marker CD86 and increased the anti-inflammatory marker CD206 on inflammatory macrophages (Figs. S10(a) and S10(b) in the ESM). Additionally, these extracellular vesicles reduced the secretion of pro-inflammatory cytokines, such as TNF-α, IL-1β, and IL-6, while promoting the release of the anti-inflammatory cytokine IL-10 (Fig. S11 in the ESM). In summary, Trained-EVs suppress the activation of key inflammatory signaling pathways and coordinately regulate inflammatory factor secretion at the protein level, thereby systematically reducing inflammatory activation in macrophages

3.5 Trained-EVs promote the polarization of $CD4^+$ T cells toward Tregs in the spleen and injury sites *in vivo*

Figure 4(a) shows a schematic diagram of the *in vivo* experimental design. Dose-gradient experiments showed that Trained-EVs at 2–3 mg/kg achieved the most pronounced recovery, defining the optimal therapeutic window (Fig. S19 in the ESM). To better understand the distribution and targeting of Trained-EVs *in vivo*, EVs were labeled with the fluorescent dye DiR and fluorescence levels in organs from SCI mice were measured to assess their biodistribution and targeting. The results show that fluorescence signals in the EVs group were mainly concentrated in the liver, followed by the spleen, which is consistent with nanoparticle clearance by the reticuloendothelial system. In contrast, both the MD-EVs and trained-EV groups exhibited fluorescence enrichment in the liver and spleen, with significant signals at the SCI site (Figs. 4(b) and 4(c)). Myelin debris, a neurospecific component, may interact with receptors in the injured microenvironment, thereby guiding the targeted migration of EVs to the SCI site.

To investigate how Trained-EVs regulate adaptive immunity in SCI mice, splenic lymphocytes were isolated at 3 dpi for flow cytometry analysis. The results show that the proportions of $CD4^+CD25^+FoxP3^+$ regulatory T cells (Tregs) and IL-4^+CD4^+ type 2 helper T cells (Th2) increased in the Trained-EVs group, while the proportions of IFN-γ^+CD4^+ type 1 helper T cells (Th1) and IL-$17A^+CD4^+$ type 17 helper T cells (Th17) decreased (Figs. 4(d) and 4(e)). These findings demonstrate that Trained-EVs boost Treg and Th2 cell proportions while reducing Th1 and Th17 differentiation, thereby reshaping the $CD4^+$ T cell subset balance and enhancing adaptive immunity in mice.

To further investigate the immune microenvironment at the injury site, immunofluorescence analysis was performed at 7 dpi to assess the aggregation of various $CD4^+$ T cell subsets in the spinal cord. The results revealed significant differences in immune cell distribution at the SCI site between Trained-EVs and PBS groups, with increased Tregs aggregation and reduced numbers of IFN-γ^+CD4^+ T cells (Figs. 4(f) and 4(g)). Additionally, the IL-4^+CD4^+ Th2 cell counts were significantly increased, whereas the IL-$17A^+CD4^+$ Th17 cell counts were notably lower than those in the PBS group (Figs. S12(a) and S12(b) in the ESM). Collectively, these findings confirm that Trained-EVs not only systemically influence immune cell differentiation but also precisely modify the immune microenvironment at the injury site, reshaping adaptive immune responses and providing dual protection for neural repair after SCI.

3.6 Trained-EVs successfully induce immune tolerance in macrophages/microglia at injury sites and reverse the expression of inflammatory factors

To evaluate the therapeutic effects of the Trained-EVs in SCI mice, the cytokine levels at the injury site were quantitatively measured using a Luminex multiplex cytokine assay at 3 and 7 dpi. The results showed that Trained-EVs exhibit significant anti-inflammatory regulatory effects at various stages of inflammation. Figures 5(a) and 5(b) provide clustered heat maps from the Luminex analysis at 3 and 7 dpi for the trained-EV and PBS groups following SCI. At the early injury stage (3 dpi), the IL-1β levels decreased while the IL-10 levels increased in the Trained-EVs group compared to PBS (Fig. 5(c)), indicating that Trained-EVs promote immune regulation early in the inflammatory response. By 7 dpi, the Trained-EVs group maintained and enhanced anti-inflammatory responses, showing significantly higher levels of IL-4 and IL-10, along with a notable decrease in pro-inflammatory cytokines, such as IL-1β, TNF-α, and IL-6, compared to PBS (Fig. 5(d)). These cytokine changes confirm that the Trained-EVs continuously modulate the cytokine network, effectively suppressing the inflammatory cascade.

To further clarify the molecular mechanisms by which Trained-EVs regulate cytokines, the transcriptional activities of NF-κB p50 and STAT3 were measured in spinal cord tissue at 3 dpi. Both NF-κB p50 and STAT3 transcriptional activities were significantly decreased in the Trained-EVs group (Fig. 5(e)), indicating that Trained-EVs suppress the synthesis and release of pro-inflammatory factors by inhibiting these transcriptional pathways. This result is consistent with the findings of the *in vitro* cell experiments.

Considering the crucial role of macrophages and microglia in the inflammatory response after SCI [41], immunofluorescence analysis was performed 7 dpi to measure the expression levels of the M1 pro-inflammatory marker iNOS and the M2 anti-inflammatory marker in the spinal cord tissue. The results showed that the Trained-EVs significantly influenced the phenotypic distribution of macrophages and microglia. Specifically, compared to other groups, the fluorescence intensity of iNOS-positive macrophages and microglia was notably decreased, while the fluorescence intensity of CD206-positive cells was considerably increased in the Trained-EVs group (Figs. 5(f)–5(i)). In summary, Trained-EVs exert a dynamic

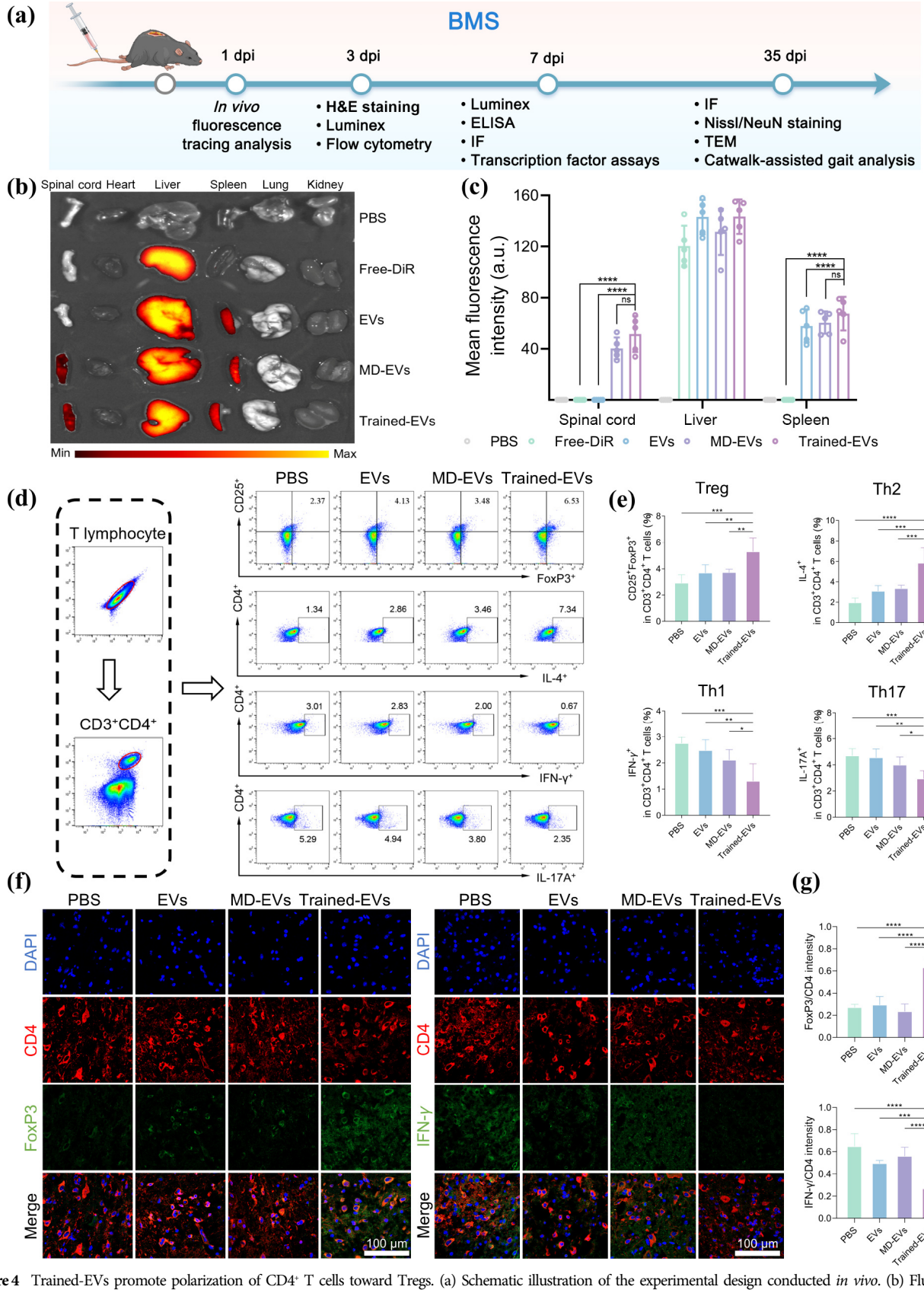

Figure 4 Trained-EVs promote polarization of $CD4^+$ T cells toward Tregs. (a) Schematic illustration of the experimental design conducted *in vivo*. (b) Fluorescence imaging and (c) statistical analysis show organ distribution of DiR-labeled EVs 24 h after tail vein injection. (d) and (e) Flow cytometry analysis and quantification reveal $CD4^+$ T cell polarization in the spleen at 3 dpi, assessing the effects of Trained-EVs ($n = 5$, mean ± SD). (f) Immunofluorescence images revealing the spatial arrangement of $CD4^+$ T cell subsets at the site of injury at 7 dpi (scale bars = 100 μm). (g) Bar graph quantifying the proportion of $CD4^+Foxp3^+$ (Tregs) and $CD4^+IFN\text{-}\gamma^+$ (Th1) cells in different groups ($n = 5$, mean ± SD). $^*P < 0.05$, $^{**}P < 0.01$, $^{***}P < 0.001$, $^{****}P < 0.0001$.

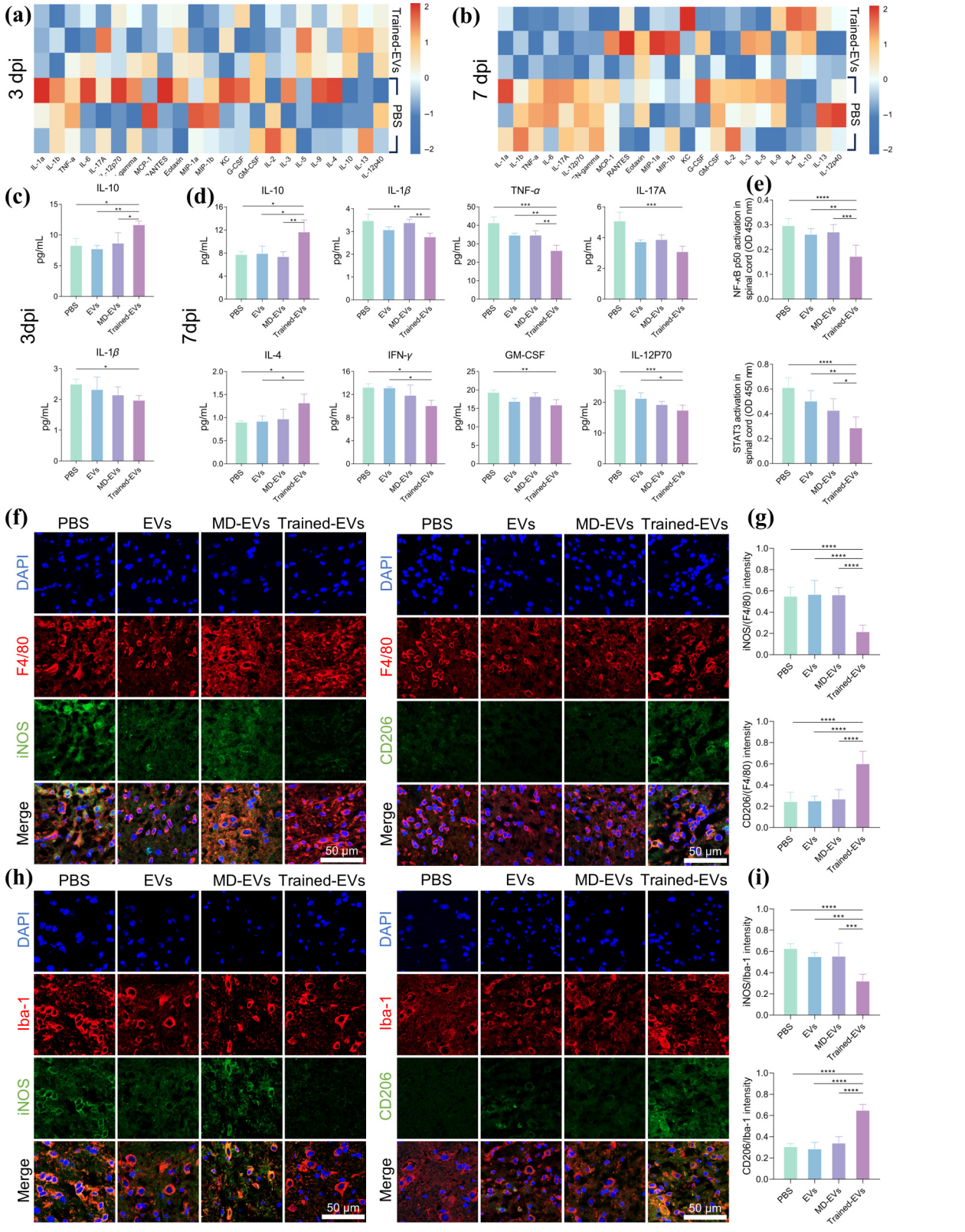

Figure 5 Trained-EVs modulate cytokine profiles and induce immune tolerance in macrophages/microglia. (a) and (b) Luminex heatmaps show differences in spinal cord cytokine expression at 3 and 7 dpi between the Trained-EVs and PBS groups (n = 3). (c) and (d) Quantification of Luminex results highlights variations in pro- and anti-inflammatory cytokine levels at 3 and 7 dpi across groups (n = 3, mean ± SD). (e) Transcription factor activity of NF-κB p50 and STAT3 in spinal cord tissue at 3 dpi (n = 5, mean ± SD). (f) and (g) Immunofluorescence images and quantitative analysis display the distribution of macrophage subtypes at the injury site at 7 dpi. Bar graphs show the proportion of F4/80$^+$iNOS$^+$ (pro-inflammatory) and F4/80$^+$CD206$^+$ (anti-inflammatory) cells (n = 5, mean ± SD). (h) and (i) Immunofluorescence images and quantitative analysis reveal the location of different microglial subtypes at the injury site. The bar graphs depict the percentage of Iba-1$^+$iNOS$^+$ and Iba-1$^+$CD206$^+$ cells (n = 5, mean ± SD). *P < 0.05, **P < 0.01, ***P < 0.001, ****P < 0.0001.

regulatory effect on the cytokine network and support the development of an anti-inflammatory immune microenvironment that favors SCI repair.

3.7 Trained-EVs promote axonal/myelin regeneration and neuronal survival at the injury site

TEM was used to analyze the myelin structure at 35 dpi to examine the effect of Trained-EVs on remyelination after SCI. The results showed that the trained-EV group had a more intact myelin structure in the spinal cord tissue (Fig. 6(a)). Several morphological parameters, including the G-ratio, myelinated axon area, diameter, and myelin thickness, were measured (Fig. 6(b)). A smaller G ratio indicates better myelin regeneration [42]. The Trained-EV group exhibited a significantly smaller G-ratio than the other groups. Additionally, the Trained-EV group showed an increased myelinated axon diameter, area, and myelin thickness in the spinal cord tissue.

Immunofluorescence analysis was conducted on the spinal cord samples at 35 dpi to evaluate the effects of the Trained-EVs. NF staining was used to assess axonal regeneration, with NF acting as a neuron-specific intermediate filament and a crucial component of the axonal structure. GFAP staining was used to investigate glial scar formation. The results showed that the trained-EV group had a higher NF fluorescence intensity and lower GFAP fluorescence intensity (Figs. 6(c) and 6(d)).

The neuroprotective effects of the Trained-EVs were further investigated. At 35 dpi, the spinal cord samples were subjected to NeuN and Nissl staining. NeuN immunohistochemical staining revealed that the trained-EV group exhibited a significantly larger dendritic area and more complex surviving neurons, indicating improved neuronal function recovery (Figs. 6(e) and 6(f)). The Nissl staining results were consistent, showing a notable increase in Nissl-positive cells in the Trained-EVs group (Figs. 6(g) and 6(h)). Additionally, the protein levels of BDNF and NT-3 in spinal cord tissue at 7 dpi were assessed using ELISA (Fig. S13 in the ESM). The BDNF and NT-3 levels were significantly higher in the trained-EV group than in the other groups.

In summary, Trained-EVs promoted remyelination, axonal regeneration, and neuronal protection, thereby improving the pathological microenvironment after SCI in multiple ways.

3.8 Behavioral experiments were conducted to evaluate the recovery of hindlimb function in spinal cord-injured mice treated with Trained-EVs

The recovery of hindlimb motor function was evaluated 35 days after treatment with Trained-EVs (Fig. S14 in the ESM). Compared with the PBS group, Trained-EVs showed significantly improved plantar stepping, weight-bearing frequency, and hind limb coordination. The BMS was used to assess recovery of motor function in mice with SCI. At 1 dpi, all subjects displayed complete hind limb paralysis, resulting in a BMS score of 0. By 35 dpi, the Trained-EV group showed significant improvement, reaching an average BMS score of 5.0 ± 0.71. The other groups displayed lower scores: MD-EVs (2.6 ± 0.55), EVs (3.0 ± 0.71), and PBS (1.8 ± 0.459). Extended behavioral evaluations up to 56 dpi revealed no further significant differences in performance beyond 35 dpi, indicating stabilization of functional recovery (Fig. 7(a)). Throughout the 35-day observation period, all groups showed comparable body weight trends up to 21 dpi. After 21 dpi, Trained-EVs-treated mice exhibited a gradual increase in body weight relative to controls, indicating good systemic tolerance and potential enhancement of overall recovery (Fig. S20 in the ESM). CatWalk gait analysis indicated that the Trained-EVs group achieved the best hindlimb recovery, with footprint patterns and stride frequency similar to the sham group and better than the other groups (Fig. 7(b)). Further assessment of the maximum contact area and contact intensity (Fig. 7(c)) showed that the Trained-EVs group had a larger maximum contact area and higher contact intensity (Figs. 7(d) and 7(e)), with no significant difference in the maximum contact intensity compared to the sham group. The footprint regularity index analysis revealed that the Trained-EVs group had a higher regularity index, indicating improved gait coordination (Figs. 7(f) and 7(g)). These results confirmed that Trained-EVs treatment significantly restored motor function in SCI mice.

To exclude hormonal confounding, serum E2 levels were quantified at 0–35 dpi. E2 levels showed normal physiological fluctuations with no significant intergroup differences, confirming that estradiol did not influence Trained-EVs-mediated recovery (Fig. S23 in the ESM).

To evaluate the biotoxicity of the Trained-EVs, H&E staining was performed on the lungs, liver, and other major organs at 3 dpi. The results showed that the major organs of the trained-EV group had normal morphology and structure, with no significant signs of damage (Fig. S15 in the ESM). To assess the potential hepatic toxicity of EVs, liver LDH and ALT activities were measured (Fig. S16 in the ESM). Importantly, no chronic toxicity was observed by 35 dpi. H&E staining of major organs (liver, spleen, lung, heart, kidney) revealed normal histology in Trained-EVs-treated mice relative to controls (Fig. S21 in the ESM). Serum ALT and LDH levels at 35 dpi remained within normal limits and showed no significant differences between groups, confirming sustained systemic safety (Fig. S22 in the ESM). These findings suggest that liver function in the Trained-EV group was similar to that in normal controls, indicating that Trained-EVs do not exhibit notable biotoxicity.

4 Discussion

Excessive inflammation following CNS injury often causes irreversible functional impairments [43]. In traumatic SCI, dysregulated innate and adaptive immune responses lead to excessive inflammation, resulting in neuronal damage and loss of function [4, 44]. Therefore, inducing tolerance in both the innate and adaptive immune responses is a key strategy for reducing excessive inflammation and creating a tolerogenic microenvironment, that promotes functional recovery after SCI [9, 10, 14]. Based on this, we developed a sequential stimulation model in which macrophages were first exposed to low-dose LPS and subsequently to myelin debris, resulting in extracellular vesicles with tolerogenic properties called Trained-EVs. This method was designed to work synergistically to induce immune tolerance in both the innate and adaptive systems, ultimately promoting functional recovery following SCI.

Previous studies have shown that high doses of LPS strongly activate immune cells, amplify inflammation, and exacerbate tissue injury [45]. Conversely, low-dose LPS induced immune tolerance, resulting in decreased cellular responsiveness to subsequent stimulation. This tolerant state is marked by the reduced

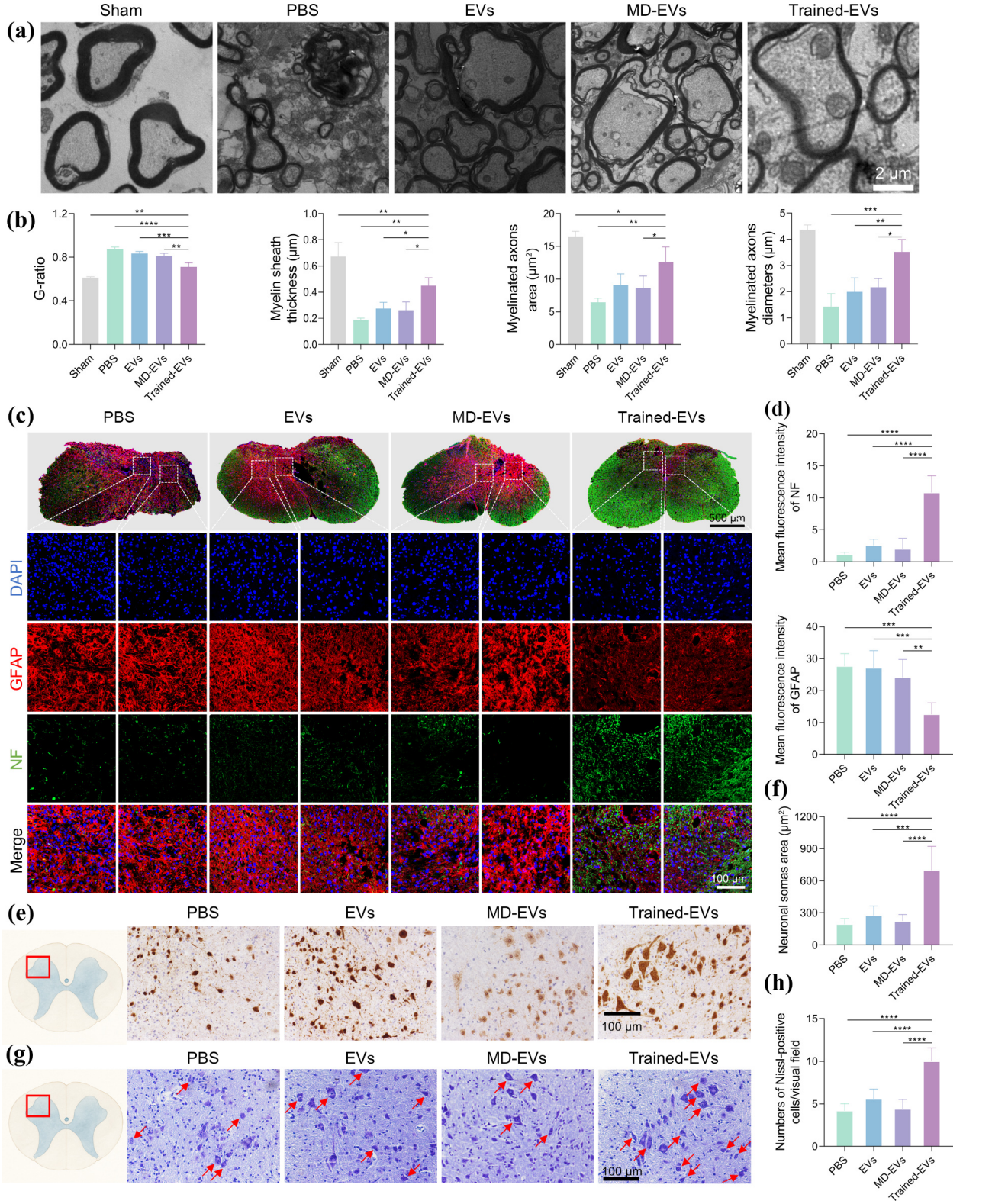

Figure 6 Trained-EVs promote axonal/myelin regeneration and neuronal survival after SCI. (a) TEM images show regenerated myelinated axons at 35 dpi (scale bar = 2 μm). (b) Quantification of myelination parameters, including g-ratio, myelin thickness, myelinated axon area, and axon diameter, in each group (n = 5, mean ± SD). (c) Immunofluorescence images of spinal cord sections at 35 dpi, stained for NF (shown in green) and GFAP (shown in red), are displayed (low magnification: scale bar = 500 μm; high magnification: scale bar = 100 μm). (d) Quantitative analysis shows the average fluorescence intensity of NF and GFAP in the lesion center (n = 5, mean ± SD). (e) and (f) Representative images of NeuN immunohistochemistry at 35 dpi and quantitative analysis show neuronal survival in the spinal cord lesion area (scale bar = 100 μm). The bar graph shows the average dendritic area of surviving neurons per field, based on five randomly selected sections per mouse (n = 5, mean ± SD). (g) and (h) Representative Nissl-stained sections at 35 dpi and quantitative analysis show neuronal morphology in the lesion area (scale bar = 100 μm). Quantification shows the average number of Nissl-positive cells per field, based on five randomly selected sections per animal (n = 5, mean ± SD). *P < 0.05, **P < 0.01, ***P < 0.001, ****P < 0.0001.

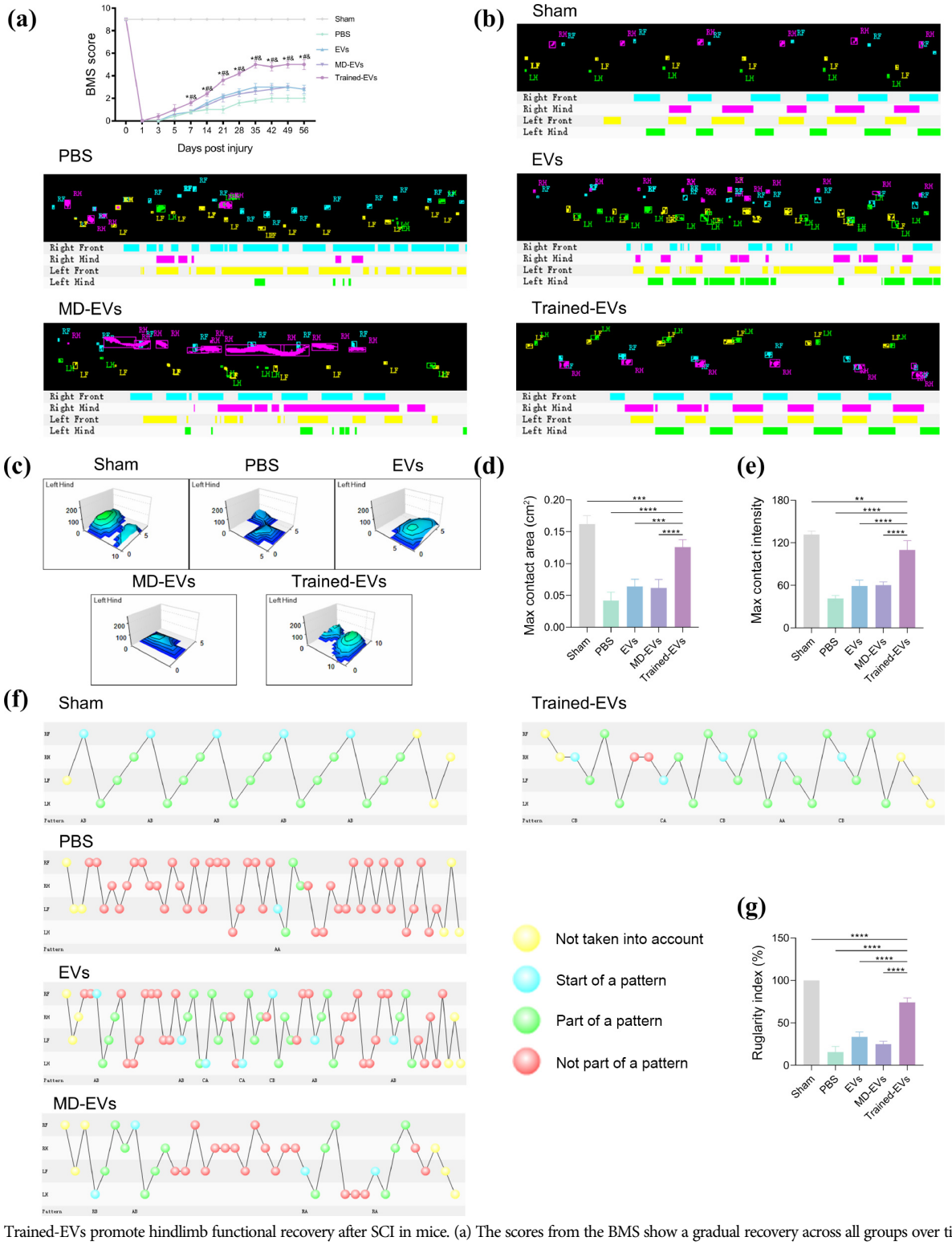

Figure 7 Trained-EVs promote hindlimb functional recovery after SCI in mice. (a) The scores from the BMS show a gradual recovery across all groups over time (two-way RM ANOVA with Dunnett's multiple comparisons: $^{*}P < 0.05$ for Trained-EVs compared to PBS; $^{\#}P < 0.05$ for Trained-EVs vs. EVs; $^{\&}P < 0.05$ for Trained-EVs against MD-EVs; $n = 5$, expressed as the mean ± SD). (b) Representative CatWalk gait images and temporal stride diagrams at 35 dpi. (c)–(e) Hindlimb paw print intensity maps and measurements of the maximum contact area and intensity of the left hind paw at 35 dpi ($n = 5$, mean ± SD). (f) and (g) Step pattern diagrams and quantification of the regularity index across groups at 35 dpi ($n = 5$, mean ± SD). $^{*}P < 0.05$, $^{**}P < 0.01$, $^{***}P < 0.001$, $^{****}P < 0.0001$.

production of pro-inflammatory cytokines and increased anti-inflammatory signals, thereby supporting immune homeostasis [46, 47]. These findings suggest that low-dose LPS can precondition macrophages toward a tolerant phenotype, prevent cytokine storms during later inflammatory phases, and provide neuroprotection to the injured spinal cord [48].

Abundant myelin debris released after SCI often aggravates inflammation and promotes an autoimmune responses [42].

Although previous studies have suggested that the administration of autoantigens after SCI can stimulate Treg induction [23], such strategies may cause further tissue damage [24]. However, our study showed that when macrophages were activated by low-dose LPS, the immunological role of myelin antigens was reprogrammed to support immune tolerance. Our results demonstrated that different doses of LPS combined with myelin debris caused macrophages to release EVs with diverse cytokine profiles. EVs produced under low-dose stimulation exhibited higher IL-10 and lower IL-1β, indicating a tolerogenic phenotype, while high-dose treatment resulted in the opposite pro-inflammatory profile. These findings suggest that the immunological properties of macrophage-derived EVs depend on the dose and are closely regulated by the strength of initial stimulation [49, 50]. EVs from macrophages preconditioned with low-dose LPS and myelin debris are rich in IL-10, and maintain tolerogenic features without the adverse effects associated with LPS or myelin debris alone [18, 19, 24]. This may be due to the inherently low immunogenicity and high biocompatibility of EVs as natural nanocarriers [26].

Conventional trained immunity is typically characterized by enhanced immune responses and is widely used in cancer therapy to boost antitumor immunity [51–53]. In contrast, Trained-EVs demonstrated a form of "negative trained immunity", marked by decreased rather than increased inflammatory responses upon secondary stimulation. This tolerogenic mode of trained immunity enables Trained-EVs to send tolerance-inducing signals, making immune responses in the damaged spinal cord more controlled and aligned with the goals of reducing inflammation and promoting neuroprotection.

In the acute phase of SCI, innate immune cells are rapidly activated and release pro-inflammatory mediators, including IL-1β and TNF-α. These events disrupt the blood–spinal cord barrier, cause secondary necrosis and apoptosis [54–56], and create a permissive environment for the subsequent amplification of adaptive immune responses. In the subacute phase, adaptive immunity becomes active, especially through the hyperactivation of Th1 and Th17 $CD4^+$ T cell subsets, which continuously secrete IFN-γ and IL-17 [57–59]. These responses further increase inflammation and suppress the repair processes, ultimately leading to chronic neuroinflammation and persistent functional deficits [60]. Our findings showed that Trained-EVs target both innate and adaptive immunity simultaneously, inducing dual immune tolerance. On one hand, Trained-EVs effectively reduced innate immune hyperactivation, proinflammatory cytokine release and acute inflammatory damage. In contrast, Trained-EVs promoted the polarization of Tregs and Th2 cells, strengthening the tolerogenic microenvironment and preventing harmful overactivation of adaptive immunity, thus creating favorable conditions for spinal cord repair.

Immune tolerance is a protective mechanism that reduces excessive immune activation, and prevents self-directed tissue damage [61]. Its main feature is hypo-responsiveness to specific antigens or stimuli, which is essential for suppressing secondary inflammation [62]. However, traditional strategies for inducing immune tolerance often carry risks of off-target effects or over-immunosuppression [63, 64]. Emerging evidence indicates that low-dose LPS exposure can induce epigenetic reprogramming in macrophages, leading to long-term tolerance. This process involves changes in chromatin accessibility and histone modifications, including decreased H3K4me3 and H3K27ac, and increased repressive marks such as H3K9me2 and H3K27me3 at promoters of inflammatory genes [10, 47, 48, 65–67]. Such remodeling silences TNF, IL-1β, and other pro-inflammatory loci while maintaining or enhancing expression of anti-inflammatory genes such as IL-10. These mechanisms have been demonstrated in both macrophages and microglia, and are now recognized as central to endotoxin tolerance and trained immunity. Our findings suggest that Trained-EVs act as natural nanocarriers capable of inducing localized immune tolerance, thus enabling targeted inflammatory control and supporting functional recovery. Taken together, the results indicate that this approach enables safe and effective therapy.

Neural regeneration and remyelination are essential for restoration of function after SCI [68]. An immune-tolerant microenvironment not only reduces inflammatory damage but also creates a supportive foundation for regeneration [69, 70]. When inflammation decreases, the levels of reparative mediators and neurotrophic signaling increase, promoting remyelination and axonal growth [71]. Immune regulation and tissue repair are interconnected and actively coordinated processes [72]. Therefore, establishing a tolerogenic microenvironment is crucial for long-term recovery after SCI [73].

In this study, Trained-EVs, as tolerance-inducing vaccines, combined the benefits of endotoxin-induced innate immune tolerance and autoantigen-driven Treg polarization. By delivering tolerance-inducing signals through EVs, both innate and adaptive immune tolerance are synergistically activated, enabling systemic regulation of inflammatory pathways and supporting neural repair and axonal regeneration. This approach offers a rapid-onset, precisely targeted, and multifaceted immunomodulatory strategy for the treatment of SCI, and shows potential as a groundbreaking immunotherapy for SCI and other CNS injuries, with significant theoretical and practical implications.

5 Conclusions

In this study, Trained-EVs were created from macrophages treated with low-dose LPS and myelin debris, which effectively induced tolerance in innate immune cells and influenced adaptive immune responses, thereby fostering a protective immune microenvironment. Our results suggest that a Trained-EVs vaccine strategy is a promising immunotherapy approach for the treatment of autoimmune and inflammatory diseases.

Electronic Supplementary Material: Supplementary material (further details of the cell morphology, RNA-seq analysis, FCM assays, CIF imaging, cytokine assays, TEM measurements, H&E staining, therapeutic window determination, NTA measurements, LDH/ALT measurements, body weight monitoring and hormone confusion effect assays) is available in the online version of this article at https://doi.org/10.26599/NR.2026.94908418.

Data availability

All data needed to support the conclusions in the paper are presented in the manuscript and the Electronic Supplementary Material. Additional data related to this paper maybe requested from the corresponding author up on request.

Acknowledgements

This work is granted by the National Natural Science Foundation of China (No. 82472421) and the National Natural Science Foundation of China (No. U23A20412).

Declaration of competing interest

The authors declare that they have no known competing financial interests or personal relationships that could have appeared to influence the work reported in this paper.

Author contribution statement

T. J.: Writing – original draft, investigation, methodology. K. R. X.: Investigation, methodology, software, writing – original draft. J. N. Z.: Visualization. J. W. S.: Visualization. J. W. N.: Methodology, investigation. X. F. L.: Visualization. F. W. Z.: Investigation. H. L. Z.: Visualization. J. L. Y.: Writing – review & editing, funding acquisition. Y. F. W.: Writing – review & editing, funding acquisition, conceptualization.

Informed consent

Not applicable.

Ethics statement

The animal experiments were carried out following the guidelines of the ethics committee of Harbin Medical University for the Care and Use of Laboratory Animals and were approved by the Committee on Ethical Use of Animals of the ethics committee of Harbin Medical University (Ethical code: SYDW2024-128).

Use of AI statement

None.

References

[1] GBD 2015 DALYs and HALE Collaborators. Global, regional, and national disability-adjusted life-years (DALYs) for 315 diseases and injuries and healthy life expectancy (HALE), 1990-2015: A systematic analysis for the Global Burden of Disease Study 2015. *Lancet* **2016**, *388*, 1603–1658.

[2] Pang, Q. M.; Chen, S. Y.; Xu, Q. J.; Fu, S. P.; Yang, Y. C.; Zou, W. H.; Zhang, M.; Liu, J.; Wan, W. H.; Peng, J. C. et al. Neuroinflammation and scarring after spinal cord injury: Therapeutic roles of MSCs on inflammation and glial scar. *Front. Immunol.* **2021**, *12*, 751021.

[3] Müller, L.; Di Benedetto, S.; Müller, V. From homeostasis to neuroinflammation: Insights into cellular and molecular interactions and network dynamics. *Cells* **2025**, *14*, 54.

[4] Liu, R.; Li, Y.; Wang, Z. Y.; Chen, P.; Xie, Y.; Qu, W. S.; Wang, M. H.; Yu, Z. Y.; Luo, X. Regulatory T cells promote functional recovery after spinal cord injury by alleviating microglia inflammation via STAT3 inhibition. *CNS Neurosci. Ther.* **2023**, *29*, 2129–2144.

[5] Brockie, S.; Hong, J.; Fehlings, M. G. The role of microglia in modulating neuroinflammation after spinal cord injury. *Int. J. Mol. Sci.* **2021**, *22*, 9706.

[6] Van Broeckhoven, J.; Sommer, D.; Dooley, D.; Hendrix, S.; Franssen, A. J. P. M. Macrophage phagocytosis after spinal cord injury: When friends become foes. *Brain* **2021**, *144*, 2933–2945.

[7] Girón, S. H.; Gómez-Lahoz, A. M.; Sanz, J. M.; Fraile-Martínez, O.; Jiménez, D. J.; Garcia-Montero, C.; de Leon-Oliva, D.; Ortega, M. A.; Atienza-Perez, M.; Diaz, D. et al. Patients with chronic spinal cord injury and a long period of evolution exhibit an altered cytokine production by CD4 and CD8 T cell populations. *Int. J. Mol. Sci.* **2023**, *24*, 7048.

[8] Jäger, A.; Dardalhon, V.; Sobel, R. A.; Bettelli, E.; Kuchroo, V. K. Th1, Th17, and Th9 effector cells induce experimental autoimmune encephalomyelitis with different pathological phenotypes. *J. Immunol.* **2009**, *183*, 7169–7177.

[9] Xi, Y.; Ma, H. F.; Liu, X.; Mu, Q. W.; An, X. Y.; Li, S.; Liang, H.; Sun, D.; Ma, R. R.; Deng, H. L. et al. Epigenetically reprogrammed nanovesicles as inverse vaccines for antigen-specific immune tolerance in autoimmune diseases. *Nano Lett.* **2025**, *25*, 6725–6734.

[10] Lajqi, T.; Lang, G. P.; Haas, F.; Williams, D. L.; Hudalla, H.; Bauer, M.; Groth, M.; Wetzker, R.; Bauer, R. Memory-like inflammatory responses of microglia to rising doses of LPS: Key role of PI3Kγ. *Front. Immunol.* **2019**, *10*, 2492.

[11] Kim, J.; Sullivan, O.; Lee, K.; Jao, J.; Tamayo, J.; Madany, A. M.; Wong, B.; Ashwood, P.; Ciernia, A. V. Repeated LPS induces training and tolerance of microglial responses across brain regions. *J. Neuroinflammation* **2024**, *21*, 233.

[12] Chen, S. H.; Han, S. Y.; Hu, C. F.; Zhou, R.; Gao, Y.; Tu, D. Z.; Gao, H. M.; Feng, J.; Wang, Y. B.; Lu, R. B. et al. Activation of the MAC1-ERK1/2-NOX2 pathway is required for LPS-induced sustaining reactive microgliosis, chronic neuroinflammation and neurodegeneration. *Antioxidants* **2022**, *11*, 1202.

[13] Yu, H. P.; Kan, J. L.; Tang, M. M.; Zhu, Y. B.; Hu, B. Y. Lipopolysaccharide preconditioning restricts microglial overactivation and alleviates inflammation-induced depressive-like behavior in mice. *Brain Sci.* **2023**, *13*, 549.

[14] Zhou, M.; Aziz, M.; Denning, N. L.; Yen, H. T.; Ma, G. F.; Wang, P. Extracellular CIRP induces macrophage endotoxin tolerance through IL-6R-mediated STAT3 activation. *JCI Insight* **2020**, *5*, e133715.

[15] Duffy, S. S.; Keating, B. A.; Perera, C. J.; Moalem-Taylor, G. The role of regulatory T cells in nervous system pathologies. *J. Neurosci. Res.* **2018**, *96*, 951–968.

[16] Docampo, M. J.; Lutterotti, A.; Sospedra, M.; Martin, R. Mechanistic and biomarker studies to demonstrate immune tolerance in multiple sclerosis. *Front. Immunol.* **2022**, *12*, 787498.

[17] Medeiros-Furquim, T.; Miedema, A.; Schilder, E.; Brouwer, N.; Holtman, I. R.; Kooistra, S. M.; Eggen, B. J. L. Microglia endotoxin tolerance is retained after enforced repopulation. *Brain Behav. Immun.* **2025**, *128*, 512–528.

[18] Kerr, A. W.; Efron, P. A.; Larson, S. D.; Rincon, J. C. T-cell activation and LPS: A dangerous duo for organ dysfunction. *J. Leukoc. Biol.* **2022**, *112*, 219–220.

[19] Bozadas, P.; Nadella, R.; Sánchez-García, A.; Rembao Bojórquez, D.; Rovirosa Hernández, M.; Hernandez Baltazar, D. Lipopolysaccharide-based endotoxemia produce toxicity in peripheral organs and microglia migration in a dose-dependent manner in rat substantia nigra. *Folia Neuropathol.* **2019**, *57*, 258–266.

[20] Sakaguchi, S.; Kawakami, R.; Mikami, N. Treg-based immunotherapy for antigen-specific immune suppression and stable tolerance induction: A perspective. *Immunother. Adv.* **2023**, *3*, ltad007.

[21] Ciurkiewicz, M.; Herder, V.; Beineke, A. Beneficial and detrimental effects of regulatory T cells in neurotropic virus infections. *Int. J. Mol. Sci.* **2020**, *21*, 1705.

[22] Wang, W. K.; Thomas, R.; Oh, J.; Su, D. M. Accumulation of pTreg cells is detrimental in late-onset (aged) mouse model of multiple sclerosis. *Aging Cell* **2022**, *21*, e13630.

[23] Fissolo, N.; Costa, C.; Nurtdinov, R. N.; Bustamante, M. F.; Llombart, V.; Mansilla, M. J.; Espejo, C.; Montalban, X.; Comabella, M. Treatment with MOG-DNA vaccines induces $CD4^+CD25^+FoxP3^+$ regulatory T cells and up-regulates genes with neuroprotective functions in experimental autoimmune encephalomyelitis. *J. Neuroinflammation* **2012**, *9*, 139.

[24] Jones, T. B.; Ankeny, D. P.; Guan, Z.; McGaughy, V.; Fisher, L. C.; Basso, D. M.; Popovich, P. G. Passive or active immunization with myelin basic protein impairs neurological function and exacerbates neuropathology after spinal cord injury in rats. *J. Neurosci.* **2004**, *24*, 3752–3761.

[25] Marar, C.; Starich, B.; Wirtz, D. Extracellular vesicles in immunomodulation and tumor progression. *Nat. Immunol.* **2021**, *22*, 560–570.
[26] Pan, S. J.; Pei, L. J.; Zhang, A. M.; Zhang, Y. H.; Zhang,2 C. L.; Huang, M.; Huang, Z. C.; Liu, B.; Wang, L. R.; Ma, L. J. et al. Passion fruit-like exosome-PMA/Au-BSA@Ce6 nanovehicles for real-time fluorescence imaging and enhanced targeted photodynamic therapy with deep penetration and superior retention behavior in tumor. *Biomaterials* **2020**, *230*, 119606.
[27] Morad, G.; Carman, C. V.; Hagedorn, E. J.; Perlin, J. R.; Zon, L. I.; Mustafaoglu, N.; Park, T. E.; Ingber, D. E.; Daisy, C. C.; Moses, M. A. Tumor-derived extracellular vesicles breach the intact blood-brain barrier via transcytosis. *ACS Nano* **2019**, *13*, 13853–13865.
[28] Sun, X.; Wang, X.; Chen, T. X.; Li, T. Y.; Cao, K.; Lu, A.; Chen, Y. X.; Sun, D. M.; Luo, J. H.; Fan, J. Q. et al. Myelin activates FAK/Akt/NF-κB pathways and provokes CR3-dependent inflammatory response in murine system. *PLoS One* **2010**, *5*, e9380.
[29] Lin, B. L.; Zhou, Y. B.; Huang, Z. H.; Ma, M.; Qi, M. H.; Jiang, Z. J.; Li, G. Y.; Xu, Y. L.; Yan, J. X.; Wang, D. et al. GPR34 senses demyelination to promote neuroinflammation and pathologies. *Cell. Mol. Immunol.* **2024**, *21*, 1131–1144.
[30] He, C.; Hu, C.; He, W. Z.; Sun, Y. C.; Jiang, Y. Z.; Liu, L.; Hou, J.; Chen, K. X.; Jiao, Y. R.; Huang, M. et al. Macrophage-derived extracellular vesicles regulate skeletal stem/progenitor cell lineage fate and bone deterioration in obesity. *Bioact. Mater.* **2024**, *36*, 508–523.
[31] Biswas, S. K.; Lopez-Collazo, E. Endotoxin tolerance: New mechanisms, molecules and clinical significance. *Trends Immunol.* **2009**, *30*, 475–487.
[32] Hu, X.; Xu, W.; Ren, Y. L.; Wang, Z. J.; He, X. L.; Huang, R. Z.; Ma, B.; Zhao, J. W.; Zhu, R. R.; Cheng, L. M. Spinal cord injury: Molecular mechanisms and therapeutic interventions. *Signal Transduct. Target. Ther.* **2023**, *8*, 245.
[33] Kopper, T. J.; Gensel, J. C. Myelin as an inflammatory mediator: Myelin interactions with complement, macrophages, and microglia in spinal cord injury. *J. Neurosci. Res.* **2018**, *96*, 969–977.
[34] Chang, J. W.; Wu, M. T.; Song, W. S.; Yang, F. Y. Ultrasound stimulation suppresses LPS-induced proinflammatory responses by regulating NF-κB and CREB activation in microglial cells. *Cereb. Cortex* **2020**, *30*, 4597–4606.
[35] Kacimi, R.; Giffard, R. G.; Yenari, M. A. Endotoxin-activated microglia injure brain derived endothelial cells via NF-κB, JAK-STAT and JNK stress kinase pathways. *J. Inflamm.* **2011**, *8*, 7.
[36] Kawai, T.; Akira, S. The role of pattern-recognition receptors in innate immunity: Update on toll-like receptors. *Nat. Immunol.* **2010**, *11*, 373–384.
[37] Shi, L. G.; Sun, Z. Y.; Su, W.; Xu, F.; Xie, D.; Zhang, Q. X.; Dai, X. J.; Iyer, K.; Hitchens, T. K.; Foley, L. M. et al. Treg cell-derived osteopontin promotes microglia-mediated white matter repair after ischemic stroke. *Immunity* **2021**, *54*, 1527–1542.e8.
[38] Gao, X.; Han, Z. H.; Huang, C.; Lei, H. L.; Li, G. Q.; Chen, L.; Feng, D. D.; Zhou, Z. J.; Shi, Q.; Cheng, L. et al. An anti-inflammatory and neuroprotective biomimetic nanoplatform for repairing spinal cord injury. *Bioact. Mater.* **2022**, *18*, 569–582.
[39] Kushwaha, S.; Saji, J.; Verma, R.; Singh, V.; Ansari, J. A.; Mishra, S. K.; Roy, O.; Patnaik, S.; Ghosh, D. Microglial neuroinflammation-independent reversal of demyelination of corpus callosum by arsenic in a cuprizone-induced demyelinating mouse model. *Mol. Neurobiol.* **2024**, *61*, 6822–6841.
[40] Fu, Y. J.; Xu, B.; Huang, S. W.; Luo, X.; Deng, X. L.; Luo, S.; Liu, C.; Wang, Q.; Chen, J. Y.; Zhou, L. Baicalin prevents LPS-induced activation of TLR4/NF-κB p65 pathway and inflammation in mice via inhibiting the expression of CD14. *Acta Pharmacol. Sin.* **2021**, *42*, 88–96.
[41] Jin, Y.; Song, Y. X.; Lin, J. Q.; Liu, T. Q.; Li, G. C.; Lai, B. Q.; Gu, Y.; Chen, G.; Xing, L. Y. Role of inflammation in neurological damage and regeneration following spinal cord injury and its therapeutic implications. *Burns Trauma* **2023**, *11*, tkac054.
[42] Li, P. F.; Liu, J. S.; Wang, Y. Y.; Li, M.; Gong, X. Q.; Peng, Z. B.; Liu, Y. S.; Zhang, Y. B.; Luan, Z. W.; Liu, D. Q. et al. Spatiotemporal targeted delivery of biomimetic bacterial outer membrane nanoparticles for enhanced spinal cord injury repair. *Adv. Mater.* **2025**, *37*, 2502795.
[43] Silver, J.; Schwab, M. E.; Popovich, P. G. Central nervous system regenerative failure: Role of oligodendrocytes, astrocytes, and microglia. *Cold Spring Harb. Perspect. Biol.* **2015**, *7*, a020602.
[44] Zrzavy, T.; Schwaiger, C.; Wimmer, I.; Berger, T.; Bauer, J.; Butovsky, O.; Schwab, J. M.; Lassmann, H.; Höftberger, R. Acute and non-resolving inflammation associate with oxidative injury after human spinal cord injury. *Brain* **2021**, *144*, 144–161.
[45] Kim, S. J.; Li, J. R. Caspase blockade induces RIP3-mediated programmed necrosis in toll-like receptor-activated microglia. *Cell Death Dis.* **2013**, *4*, e716.
[46] Mizobuchi, H.; Soma, G. I. Low-dose lipopolysaccharide as an immune regulator for homeostasis maintenance in the central nervous system through transformation to neuroprotective microglia. *Neural Regen. Res.* **2021**, *16*, 1928–1934.
[47] Novakovic, B.; Habibi, E.; Wang, S. Y.; Arts, R. J. W.; Davar, R.; Megchelenbrink, W.; Kim, B.; Kuznetsova, T.; Kox, M.; Zwaag, J. et al. *β*-Glucan reverses the epigenetic state of LPS-induced immunological tolerance. *Cell* **2016**, *167*, 1354–1368.
[48] Seeley, J. J.; Ghosh, S. Molecular mechanisms of innate memory and tolerance to LPS. *J. Leukoc. Biol.* **2017**, *101*, 107–119.
[49] Zhao, S. L.; Mi, Y. S.; Guan, B. J.; Zheng, B. B.; Wei, P.; Gu, Y. Z.; Zhang, Z. X.; Cai, S. J.; Xu, Y.; Li, X. X. et al. Tumor-derived exosomal miR-934 induces macrophage M2 polarization to promote liver metastasis of colorectal cancer. *J. Hematol. Oncol.* **2020**, *13*, 156.
[50] Xu, R.; Greening, D. W.; Zhu, H. J.; Takahashi, N.; Simpson, R. J. Extracellular vesicle isolation and characterization: Toward clinical application. *J. Clin. Invest.* **2016**, *126*, 1152–1162.
[51] Liu, G. N.; Ma, N. N.; Cheng, K. M.; Feng, Q. Q.; Ma, X. T.; Yue, Y. L.; Li, Y.; Zhang, T. J.; Gao, X. Y.; Liang, J. et al. Bacteria-derived nanovesicles enhance tumour vaccination by trained immunity. *Nat. Nanotechnol.* **2024**, *19*, 387–398.
[52] Ding, C. L.; Shrestha, R.; Zhu, X. J.; Geller, A. E.; Wu, S. Z.; Woeste, M. R.; Li, W. Q.; Wang, H. M.; Yuan, F.; Xu, R. B. et al. Inducing trained immunity in pro-metastatic macrophages to control tumor metastasis. *Nat. Immunol.* **2023**, *24*, 239–254.
[53] Ziogas, A.; Bruno, M.; van der Meel, R.; Mulder, W. J. M.; Netea, M. G. Trained immunity: Target for prophylaxis and therapy. *Cell Host Microbe* **2023**, *31*, 1776–1791.
[54] Chio, C. C.; Lin, M. T.; Chang, C. P. Microglial activation as a compelling target for treating acute traumatic brain injury. *Curr. Med. Chem.* **2015**, *22*, 759–770.
[55] Hernández, J.; Francos-Quijorna, I.; Redondo-Castro, E.; López-Vales, R.; Navarro, X. Microglia stimulation by protein extract of injured rat spinal cord. A novel in vitro model for studying activated microglia. *Front. Mol. Neurosci.* **2021**, *14*, 582497.
[56] Zhou, H. Y.; Wang, X.; Li, Y.; Wang, D.; Zhou, X. Z.; Xiao, N.; Li, G. X.; Li, G. Dynamic development of microglia and macrophages after spinal cord injury. *Neural Regen. Res.* **2025**, *20*, 3606–3619.
[57] Liu, S. Y.; Qiao, H. W.; Song, T. B.; Liu, X. L.; Yao, Y. X.; Zhao, C. S.; Barret, O.; Xu, S. L.; Cai, Y. N.; Tamagnan, G. D. et al. Brain microglia activation and peripheral adaptive immunity in Parkinson's disease: A multimodal PET study. *J. Neuroinflammation* **2022**, *19*, 209.
[58] Wang, S. K.; Li, G. L.; Liang, X. J.; Wu, Z. X.; Chen, C.; Zhang, F. W.; Niu, J. W.; Li, X. F.; Yan, J. L.; Wang, N. X. et al. Small extracellular vesicles derived from altered peptide ligand-loaded dendritic cell act as a therapeutic vaccine for spinal cord injury through eliciting $CD4^+$ T cell-mediated neuroprotective immunity. *Adv. Sci.* **2024**, *11*, 2304648.
[59] Savarin, C.; Hinton, D. R.; Valentin-Torres, A.; Chen, Z. H.; Trapp, B.

D.; Bergmann, C. C.; Stohlman, S. A. Astrocyte response to IFN-γ limits IL-6-mediated microglia activation and progressive autoimmune encephalomyelitis. *J. Neuroinflammation* **2015**, *12*, 79.

[60] An, J.; Yin, J. J.; He, Y.; Sui, R. X.; Miao, Q.; Wang, Q.; Yu, J. Z.; Yu, J. W.; Shi, F. D.; Ma, C. G. et al. Temporal and spatial dynamics of astroglial reaction and immune response in cuprizone-induced demyelination. *Neurotox. Res.* **2020**, *37*, 587–601.

[61] Han, L.; Wu, T. X.; Zhang, Q.; Qi, A. N.; Zhou, X. H. Immune tolerance regulation is critical to immune homeostasis. *J. Immunol. Res.* **2025**, *2025*, 5006201.

[62] Gu, Y.; Ye, T.; Tan, P. P.; Tong, L. J.; Ji, J. L.; Gu, Y. M.; Shen, Z. X.; Shen, X. H.; Lu, X.; Huang, C. Tolerance-inducing effect and properties of innate immune stimulation on chronic stress-induced behavioral abnormalities in mice. *Brain Behav. Immun.* **2021**, *91*, 451–471.

[63] Meng, C. Y.; Sun, S. Y.; Liang, Y.; Xu, H. R.; Zhang, C.; Zhang, M.; Wang, F. S.; Fu, Y. X.; Peng, H. Engineered anti-PDL1 with IFNα targets both immunoinhibitory and activating signals in the liver to break HBV immune tolerance. *Gut* **2023**, *72*, 1544–1554.

[64] Oberholtzer, N.; Atkinson, C.; Nadig, S. N. Adoptive transfer of regulatory immune cells in organ transplantation. *Front. Immunol.* **2021**, *12*, 631365.

[65] Chen, S. Y.; Yang, J.; Wei, Y. Q.; Wei, X. W. Epigenetic regulation of macrophages: From homeostasis maintenance to host defense. *Cell. Mol. Immunol.* **2020**, *17*, 36–49.

[66] Foster, S. L.; Hargreaves, D. C.; Medzhitov, R. Gene-specific control of inflammation by TLR-induced chromatin modifications. *Nature* **2007**, *447*, 972–978.

[67] Netea, M. G.; Domínguez-Andrés, J.; Barreiro, L. B.; Chavakis, T.; Divangahi, M.; Fuchs, E.; Joosten, L. A. B.; van der Meer, J. W. M.; Mhlanga, M. M.; Mulder, W. J. M. et al. Defining trained immunity and its role in health and disease. *Nat. Rev. Immunol.* **2020**, *20*, 375–388.

[68] Papastefanaki, F.; Matsas, R. From demyelination to remyelination: The road toward therapies for spinal cord injury. *Glia* **2015**, *63*, 1101–1125.

[69] Emmerich, K.; White, D. T.; Kambhampati, S. P.; Casado, G. L.; Fu, T. M.; Chunawala, Z.; Sahoo, A.; Nimmagadda, S.; Krishnan, N.; Saxena, M. T. et al. Nanoparticle-based targeting of microglia improves the neural regeneration enhancing effects of immunosuppression in the zebrafish retina. *Commun. Biol.* **2023**, *6*, 534.

[70] Yao, X. Y.; Kong, L. C.; Qiao, Y.; Brand, D.; Li, J. H.; Yan, Z. W.; Zheng, S. G.; Qian, Y.; Fan, C. Y. Schwann cell-secreted frizzled-related protein 1 dictates neuroinflammation and peripheral nerve degeneration after neurotrauma. *Cell Rep. Med.* **2024**, *5*, 101791.

[71] Ren, J.; Zhu, B.; Gu, G. J.; Zhang, W. C.; Li, J. J.; Wang, H. D.; Wang, M.; Song, X. M.; Wei, Z. J.; Feng, S. Q. Schwann cell-derived exosomes containing MFG-E8 modify macrophage/microglial polarization for attenuating inflammation via the SOCS3/STAT3 pathway after spinal cord injury. *Cell Death Dis.* **2023**, *14*, 70.

[72] Xu, Z. H.; Wu, L.; Tang, Y.; Xi, K.; Tang, J. C.; Xu, Y. C.; Xu, J. Z.; Lu, J.; Guo, K. J.; Gu, Y. et al. Spatiotemporal regulation of the bone immune microenvironment via dam-like biphasic bionic periosteum for bone regeneration. *Adv. Healthc. Mater.* **2023**, *12*, 2201661.

[73] O'Shea, T. M.; Ao, Y.; Wang, S. N.; Ren, Y. L.; Cheng, A. L.; Kawaguchi, R.; Shi, Z. C.; Swarup, V.; Sofroniew, M. V. Derivation and transcriptional reprogramming of border-forming wound repair astrocytes after spinal cord injury or stroke in mice. *Nat. Neurosci.* **2024**, *27*, 1505–1521.